

# Recent Changes in the Earth's Core Magnetic Field

Master's Thesis

Christian Ledertoug Vogel  
Juni 2016

Supervisor:  
Chris Finlay

DTU Space  
National Space Institute

---

## Abstract

In this thesis, a time-dependent model of the Earth's core magnetic field spanning the years 2000-2016 is developed using data from the global network of magnetic ground observatories, and from the CHAMP and Swarm satellite missions. The spatial representation is based on a grid of equal area distributed monopoles on the surface of a sphere, placed within the Earth's core. The temporal representation is based on covariance functions, because their great flexibility allows for a more "rough" time-dependence than the spline basis functions that are traditionally adopted. The localized nature of the monopole representation, along with a regularization based on minimizing the L1-norm of the radial field at the core surface, was tested. The aim is to represent sparse features in the main field at the core mantle boundary, that would otherwise be smoothed out in conventional models based on spherical harmonics. This regularization scheme was however unsuccessful, so a more simple L2-regularization of the monopole amplitudes was performed instead. The resulting model had a satisfactory weighted RMS misfit, and was generally in very good agreement with results from the earlier models CHAOS-5 and CHAOS-6, which used similar data sets, but a completely different modelling scheme. Investigating the changes in the unsigned flux during the model time span, we found that only a change of 1.4% in the course of 16 years was evident.

# Contents

<b>1</b>	<b>Introduction</b>	<b>4</b>
<b>2</b>	<b>Introduction to geomagnetism</b>	<b>6</b>
2.1	The core field . . . . .	6
2.2	The crustal field . . . . .	11
2.3	The external and externally induced fields . . . . .	13
2.4	Modelling the geomagnetic field . . . . .	15
<b>3</b>	<b>Measurements and data selection</b>	<b>19</b>
3.1	Ground observatories . . . . .	19
3.2	The CHAMP satellite . . . . .	21
3.3	The Swarm satellite trio . . . . .	22
3.4	Satellite data selection criteria . . . . .	22
<b>4</b>	<b>Method</b>	<b>24</b>
4.1	The monopole forward modelling scheme . . . . .	24
4.2	Distribution of points on a sphere and integrating on the sphere . . . . .	25
4.2.1	Recursive zonal equal area sphere partitioning . . . . .	26
4.2.2	Lebedev Quadrature . . . . .	28
4.3	Modelling time dependence using temporal covariance functions . . . . .	28
4.3.1	A time-dependent design matrix . . . . .	29
4.3.2	Modelling the secular variation. . . . .	30
4.4	Solving the inverse problem . . . . .	31
4.4.1	L2 regularized inversion . . . . .	31
4.4.2	Estimation of prior data errors from covariances . . . . .	32
4.4.3	L1 inversion for a sparse model . . . . .	33
4.5	Choice of the modelling hyperparameters . . . . .	34
4.5.1	Configuration of the monopole grid . . . . .	34
4.5.2	Covariance function and characteristic time scale $\tau$ . . . . .	38
4.5.3	Regularization parameter $\alpha^2$ . . . . .	41
<b>5</b>	<b>Results</b>	<b>42</b>
5.1	A time-dependent L2-regularized monopole-based field model . . . . .	42
5.2	L1-regularized monopole-based field model . . . . .	47

**6 Discussion** **49**  
6.1 Comparison with CHAOS models . . . . . 49  
6.2 Changes in the unsigned flux . . . . . 53

**7 Conclusion** **56**

**References** **58**

**A Matlab code** **61**  
A.1 Time-dependent design matrix . . . . . 61  
A.2 L2-regularized inversion . . . . . 62  
A.3 Static L1-regularized inversion . . . . . 66

# Chapter 1

## Introduction

Magnetism as a natural phenomenon has been known to mankind for over a thousand years, the ancient Greeks described the ability of the so-called "lodestones" to attract iron. Around the turn of the first millennium, Chinese scholars invented the compass by placing one such lodestone in a bowl of water, and noticed that it turned to face south. The invention spread to Europe and became the most important tool for navigation at sea, and it quickly became known that the north measured by compasses differed slightly from true north by an angle called the declination. It was also observed that a compass needle free to rotate in any direction would point not only towards north, but also slightly downwards, in an angle called the inclination. There was not much more knowledge gained on the subject until the year 1600, when Sir William Gilbert published a book called "De Magnete" (Latin for On Magnets), in which he postulated that the reason compass needles pointed north was because the Earth was itself a giant magnet (Stern, 2002).

Other important discoveries came in the following years, as for example the secular variation of the declination by Henry Gellibrand in 1634, but it was not until the 1830s when Gauss devoted time to the study of geomagnetism that any understanding of the causes of these phenomenon or a mathematical description of them was gained. Gauss made three great contributions to the to field of geomagnetism: He invented the first procedure for making absolute measurements of the magnetic field. He, along with his student Wilhelm Weber, spearheaded the formation of the Göttingen Magnetic Union, an international network of geomagnetic observatories that made systematic measurements of the magnetic elements and their time changes. The third contribution was his 1838 paper "Allgemeine Theorie des Erdmagnetismus", where he formulated his idea of expanding the magnetic potential field as a sum of spherical harmonics, laying the foundation for modern geomagnetic field modelling. His theory allowed for the separation of internal and external sources, from which he deduced that the vast majority of the geomagnetic field was of internal origin and resembling that of a magnetic dipole. This part of the field is now referred to as the core field, and modelling the core field is the primary concern of this thesis. (Garland, 1979).

A wealth of knowledge on the geomagnetic field has been gained since Gauss, particularly since the age of satellites has provided truly global coverage to geomagnetic field measurements on a scale simply not possible with stationary observatories. Several distinct sources of both internal and external origin have been identified, and each of these contribute to the total field measured by our equipment, a subject that will be elaborated on further in chapter

2. This is done since careful separation of different field sources is a necessity when modelling the core field. An impression of the current state of geomagnetic field modelling will also be provided. Now, almost 200 years later, Gauss' method of expressing the geomagnetic field in terms of spherical harmonics is still standard practice. This thesis however, will use an analogous representation of magnetic monopole sources equal area distributed on the surface of a sphere, located within the Earth's core.

Chapter 3 will describe the dataset provided by the INTERMAGNET network of geomagnetic observatories, as well as give short descriptions of the CHAMP and Swarm satellites and the data they provide. This chapter will also include an explanation of the selection criteria that the data has been subjected to.

Chapter 4 will provided a detailed explanation of the monopole forward modelling scheme, as well as how time-dependence is modelled by temporal covariance functions. This chapter also explains how the inverse problem is regularized and solved to derive the model parameters, and how the appropriate modelling hyperparameters are determined through a series of test cases.

Chapter 5 summarizes the results of the model with all the relevant figures, and chapter 6 compares these results with those of the CHAOS-5 and CHAOS-6 models. Chapter 6 also includes an investigation of the changes in the unsigned flux of the model, since this is of relevance to a debate in internal field modelling that is currently ongoing. Chapter 7 concludes the thesis and provides an outlook further study.

# Chapter 2

## Introduction to geomagnetism

At any point in space near Earth, the magnetic field that is felt and measured will be a superposition of field contributions from different sources, all of which have highly different amplitudes and wavelengths. It is therefore important to have some knowledge of these sources in order to accurately separate them, so that the core field can be modelled with as little contamination from other sources as possible. It is common to differentiate between two different types of magnetic field sources: Internal and external ones, meaning located within the Earth or more than 100 km above it. There are three distinct sources of internal origin, being the core field (sometimes called the main field), the lithospheric field and a small field contribution from the movement of the Earth's oceans. The external field consists of electrical currents within the ionosphere and magnetosphere, which also cause externally induced internal fields, see figure 2.1 (Olsen, Hulot, & Sabaka, 2014). The following sections will provide descriptions of the geomagnetic field sources and attempt to explain what causes them, with special emphasis on the core field and the geodynamo process that drives it. The chapter is concluded by a description of the CHAOS series of models, in order to give the reader an impression of the current state of geomagnetic field modelling.

### 2.1 The core field

More than 95% of the Earth's magnetic field is due to the movement of electrically conducting material in the liquid part of the Earth's core, the so-called geodynamo. A dynamo is a mechanism that converts kinetic energy into electrical energy: A simple example is the Bullard disk dynamo. The dynamo consists of an electrically conducting disk that rotates on an axle when torque is applied. If an ambient magnetic field is present, a potential difference will arise between the axle and the edge of the disc, and if a wire is joined between them, a current will flow, resulting in an axial magnetic field. If the disk spins sufficiently fast for the magnetic field to become as strong as the ambient field, the system is self-sufficient and becomes a dynamo, see figure 2.2 (Olsen & Finlay, 2015).

A similar process is thought to occur in the Earth's liquid outer core, which is composed primarily of an iron-nickel alloy, an effective conductor. This fluid is incredibly hot, and these high temperatures cause the liquid outer core to be vigorously convecting, which means that we have an electrical conductor moving through an ambient magnetic field, making dynamo

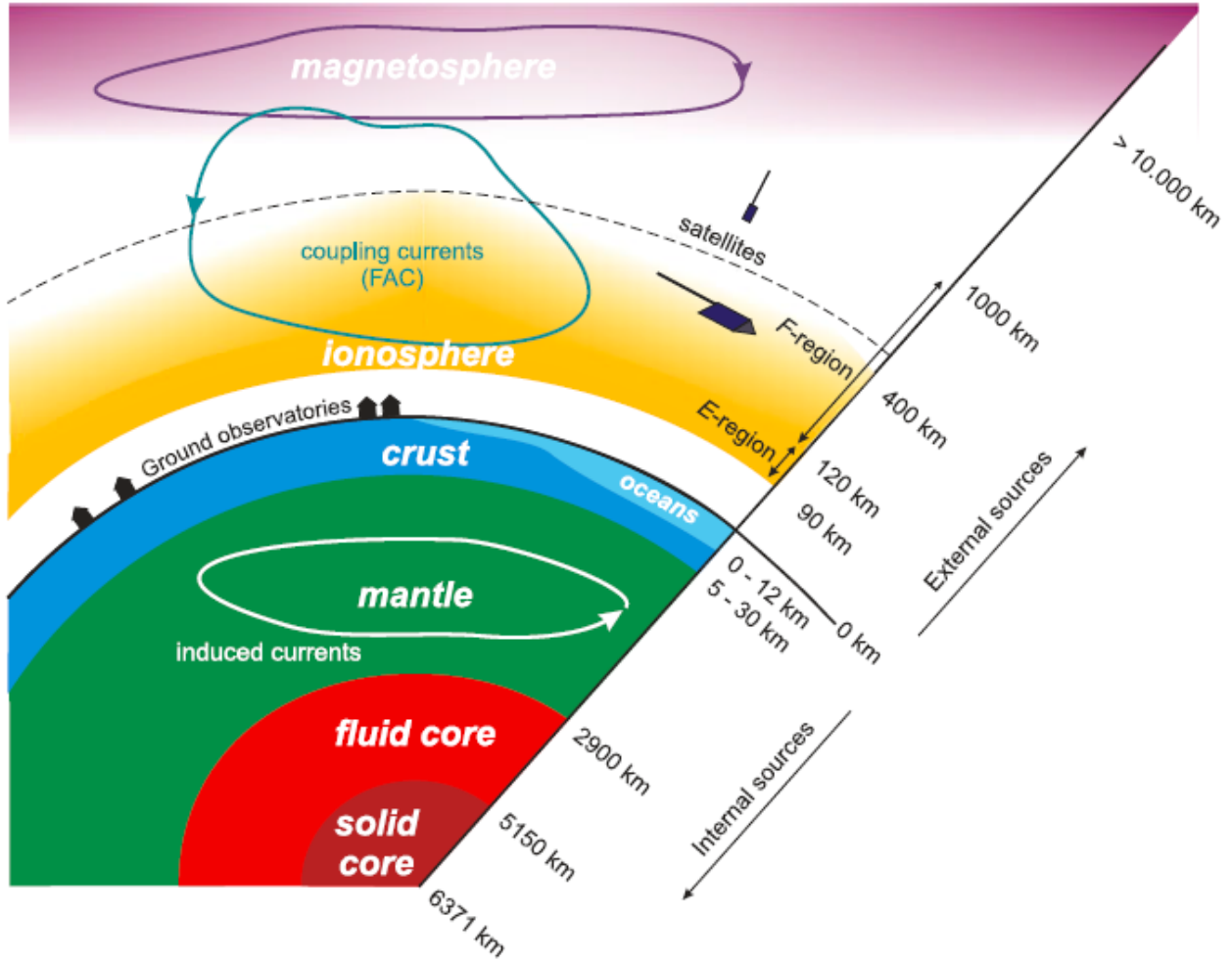


Figure 2.1: A sketch of the different sources contributing to the Earth's magnetic field. Figure from Olsen, Hulot, and Sabaka (2014)

action possible. Consider a conductor (with conductivity  $\sigma$ ) moving with speed  $\mathbf{v}$  through a magnetic field  $\mathbf{B}$ , this causes a current to run as described by Ohm's law

$$\mathbf{J} = \sigma(\mathbf{E} + \mathbf{v} \times \mathbf{B}) . \quad (2.1)$$

Dividing with  $\sigma$  and taking the curl gives us

$$\frac{1}{\sigma} \nabla \times \mathbf{J} = \nabla \times \mathbf{E} + \nabla \times (\mathbf{v} \times \mathbf{B}) . \quad (2.2)$$

If we then remember Faraday's law

$$\frac{\partial \mathbf{B}}{\partial t} = -\nabla \times \mathbf{E} , \quad (2.3)$$

and Ampere's law without displacement current

$$\nabla \times \mathbf{B} = \mu \mathbf{J} , \quad (2.4)$$

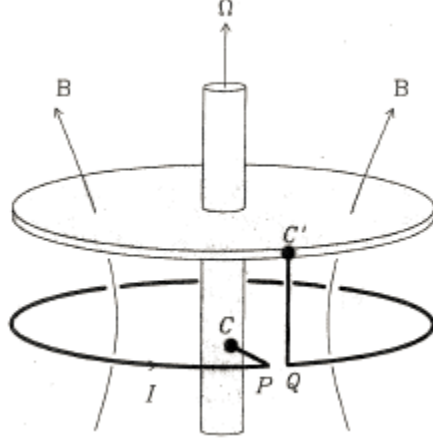


Figure 2.2: A schematic representation of the Bullard disk dynamo. A wire makes contact to the axle at C and the disk at C', it carries a current I, which causes a magnetic field B. From Olsen and Finlay (2015).

then equation (2.2) can be rewritten to eliminate  $\mathbf{J}$  and  $\mathbf{E}$

$$\frac{1}{\sigma\mu} \nabla \times \nabla \times \mathbf{B} = -\frac{\partial \mathbf{B}}{\partial t} + \nabla \times (\mathbf{v} \times \mathbf{B}) . \quad (2.5)$$

Utilizing the vector identity

$$\nabla \times \nabla \times \mathbf{B} = \nabla(\nabla \cdot \mathbf{B}) - \nabla^2 \mathbf{B} , \quad (2.6)$$

and the fact that the magnetic field is divergence free ( $\nabla \cdot \mathbf{B} = 0$ ), enables us to rewrite equation (2.5) into the magnetic induction equation

$$\frac{\partial \mathbf{B}}{\partial t} = \nabla \times (\mathbf{v} \times \mathbf{B}) + \eta \nabla^2 \mathbf{B} . \quad (2.7)$$

Here  $\eta = \frac{1}{\sigma\mu}$  is called the diffusivity. The equation has two terms: The first is the induction term, which controls the production of the magnetic field necessary to drive the dynamo, and the second is the diffusion term, which tells us how the magnetic field decays. Because of the high temperatures in the core, setting the permeability to be equal to the value in vacuum is a good approximation, which means that the magnetic induction equation can tell us the development of the Earth's magnetic field in time from the velocity and conductivity of the liquid in the outer core.

Some insight can be gained by regarding the induction equation in two extreme cases. The first case is with no movement of the conducting liquid, i.e.  $\mathbf{v} = 0$ . This leaves us with a diffusion equation

$$\frac{\partial \mathbf{B}}{\partial t} = \eta \nabla^2 \mathbf{B} . \quad (2.8)$$

When solved for a spherical conducting core with an insulating mantle, the field is found to decay in time as

$$\mathbf{B} \propto \exp\left(\frac{-\pi^2 \eta t}{a^2}\right) \quad (2.9)$$

with  $a$  being the radius of the core, approximately 3500 km. Inserting an approximate value of  $\sigma = 5 \cdot 10^5 \text{ S m}^{-1}$  for the core conductivity and using the permeability of free space ( $\mu_0 = 4\pi \cdot 10^{-7} \text{ Tm A}^{-1}$ ), the magnetic field is found to decay by a factor of  $e$  in approximately 20,000 years. Since there exists evidence that suggests that the Earth's magnetic field has existed for at least  $3 \cdot 10^9$  years, diffusion is clearly not enough to explain the observed magnetic field. There needs to be an energy source driving the dynamo in order to maintain the field, so there has to be a non-zero velocity of the conducting fluid (Jones, 2007).

The second extreme case to consider is the case of infinite conductivity, i.e.  $\eta = 0$ . The magnetic flux  $\Phi$  through some surface  $S$  is defined as

$$\Phi = \iint \mathbf{B} \cdot d\mathbf{S} . \quad (2.10)$$

The time derivative is then

$$\frac{\partial \phi}{\partial t} = \iint \frac{\partial \mathbf{B}}{\partial t} \cdot d\mathbf{S} + \int \mathbf{B} \cdot (\mathbf{v} \times d\mathbf{l}) . \quad (2.11)$$

Using the vector identity  $(\mathbf{a} \times \mathbf{b}) \cdot \mathbf{c} = -\mathbf{b} \cdot (\mathbf{a} \times \mathbf{c})$ , the last term can be rewritten as

$$\int \mathbf{B} \cdot (\mathbf{v} \times d\mathbf{l}) = - \int (\mathbf{v} \times \mathbf{B}) \cdot d\mathbf{l} . \quad (2.12)$$

This line integral can then be rewritten as a surface integral using Stoke's theorem

$$- \int (\mathbf{v} \times \mathbf{B}) \cdot d\mathbf{l} = - \iint \nabla \times (\mathbf{v} \times \mathbf{B}) \cdot d\mathbf{S} . \quad (2.13)$$

Equation (2.11) now reads

$$\frac{\partial \phi}{\partial t} = \iint \frac{\partial \mathbf{B}}{\partial t} - \nabla \times (\mathbf{v} \times \mathbf{B}) \cdot d\mathbf{S} , \quad (2.14)$$

but since  $\eta = 0$ , the induction equation tells us that

$$\frac{\partial \mathbf{B}}{\partial t} = \nabla \times (\mathbf{v} \times \mathbf{B}) \cdot d\mathbf{S} , \quad (2.15)$$

so that the time derivative of the flux equals zero, i.e. the flux is constant. So the magnetic flux passing through a surface moving along with the liquid is conserved, the magnetic field lines moves together with the fluid, and the flux is said to be "frozen in", which is why this case is called the frozen flux approximation.

To test the validity of this approximation, one can calculate the so called magnetic Reynolds ( $R_m$ ) number, defined as the ratio between the induction and diffusion terms

$$R_m = \frac{|\nabla \times (\mathbf{v} \times \mathbf{B})|}{|\eta \nabla^2 \mathbf{B}|} . \quad (2.16)$$

More induction relative to diffusion is a necessary condition for dynamo action, meaning that the magnetic Reynolds number needs to be greater than 1, and for the frozen flux

approximation to hold,  $R_m$  must be much larger than 1. A simple scale analysis can be performed to estimate the values of  $R_m$  by replacing the spatial derivatives with a division by  $L$ , some typical length scale, and replacing the vector quantities  $\mathbf{v}$  and  $\mathbf{B}$  with scalar approximations  $B$  and  $V$

$$R_m = \frac{VB/L}{\eta B/L^2} = \frac{VL}{\eta} = \mu_0 \sigma LV . \quad (2.17)$$

The fluid velocity can be estimated by studying the secular variation, leading to an approximate value of  $4 \cdot 10^{-4}$  m/s, and if a typical length scale in the core is said to be 1000 km, then  $R_m \approx 250$ , meaning that the frozen flux approximation should hold for large scale core motions and a geodynamo process is possible (Olsen & Finlay, 2015). This result is however controversial, as there are some researchers, for example Bloxham and Gubbins (1986) and Chulliat and Olsen (2010), who doubt the validity of the frozen flux approximation, as they observe non-negligible amounts of diffusion in their core field models. Other researchers, such as Jackson et al. (2007) and Wardinski and Lesur (2012), have successfully implemented frozen flux constraints in their models, suggesting that the approximation holds. Whether or not this is the case is extremely important, as the frozen flux approximation is widely used in interpreting the geomagnetic secular variation, since it can be used to directly link the movements of the magnetic field lines to the flow of conducting material in the outer core.

Our scale analysis of the magnetic induction equation has revealed that dynamo action in the core is possible, but what energy source is driving the dynamo? It is believed that there are two major sources of this energy. The first is the fact that the Earth is slowly cooling down from its initially extremely hot state, when first formed by accretion together with the rest of the solar system, causing the fluid to convect. Another source is the freezing of the liquid outer core to the solid inner core. This process releases light elements from the Fe-Ni alloy, which rise upwards, further strengthening the convection. These convective flows are distorted by the Coriolis effect due to the relatively rapid rotation of the Earth, ultimately producing flow patterns which act as a dynamo (Jones, 2007).

The field at the Earth's surface produced by the core geodynamo is largely like that of a dipole at the centre of the Earth, with its axis inclined to the axis of Earth's rotation by 10%. Its amplitude ranges from about 60,000 nT at the poles, to 30,000 nT at the equator. The field changes on time scales of years to decades, the so called secular variation. The field does have more complex small scale structure and features evolving on shorter time scales, but the small spatial features are masked by the lithospheric field, and the high-frequency parts of the core field are screened by the less conductive mantle (Olsen, Hulot, & Sabaka, 2014).

An investigation of the secular variation over a period of 400 years made from historical records by Jackson et al. (2000) revealed some characteristic aspects. One of these is the westward drift of field features, which can clearly be seen when comparing maps of the magnetic declination (the angle between the magnetic north pole and the geographic one) for different time periods, see figure 2.4. The line of zero declination which cuts the African continent in half at AD 1590 has moved to South America in AD 1990. Another prominent aspect of the secular variation is the decay of the axial dipole part of the field, the intensity being reduced by approximately 5% each century. Although the quality of the data before 1840

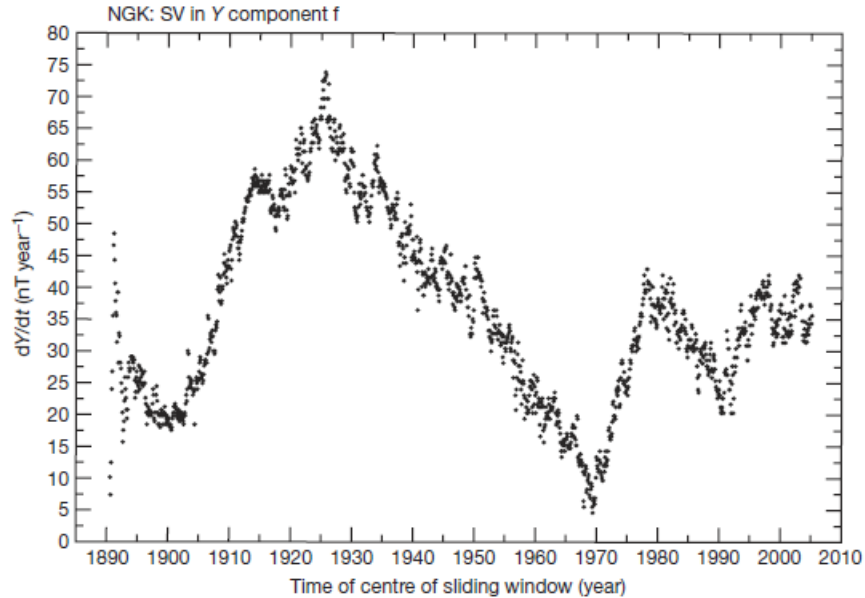


Figure 2.3: Central differences of the monthly mean values of the Y-component of the magnetic field, as measured by the Niemegek observatory in Germany. From Jackson and Finlay (2015).

makes it hard to make conclusive statements about the rate of the decay, most models after 1840 agree on a decay rate of approximately 12 nT/year.

Also a distinct feature of the secular variation are the so called geomagnetic jerks, which are abrupt changes in the second time derivative of the geomagnetic field, also called the secular acceleration. These jerk events seem to separate periods of linear change in the secular variation, and have occurred several times during the twentieth century: in 1901, 1913, 1925, 1969, 1978, 1991 and 1999. They are very clearly visible when looking at time series of some ground observatory measurements, see figure 2.3 for an example. The jerks are not always observed globally, and they are not completely simultaneous when measured at different locations across the Earth. The physical processes in the core that gives rise to these jerk events are poorly understood, although some explanations in terms of core dynamics exist (Jackson & Finlay, 2015).

## 2.2 The crustal field

The crustal field or the lithospheric field, is the second most significant internal contribution, even if it only amounts to a few percent of the total field at the Earth's surface. This field is due to the magnetization of ferromagnetic material in the Earth's crust. This can only be achieved very close to the Earth's surface, as a material loses its magnetic properties once it is heated above a certain point called the Curie temperature, and since the temperature of the Earth's crust increases with depth. The Curie points of the two most abundant magnetic minerals in the Earth's crust are 580°C and 670°C and this is usually reached at a depth of approximately 30 km on the continents and 6-7 km in the oceans (Thébaud et al.,

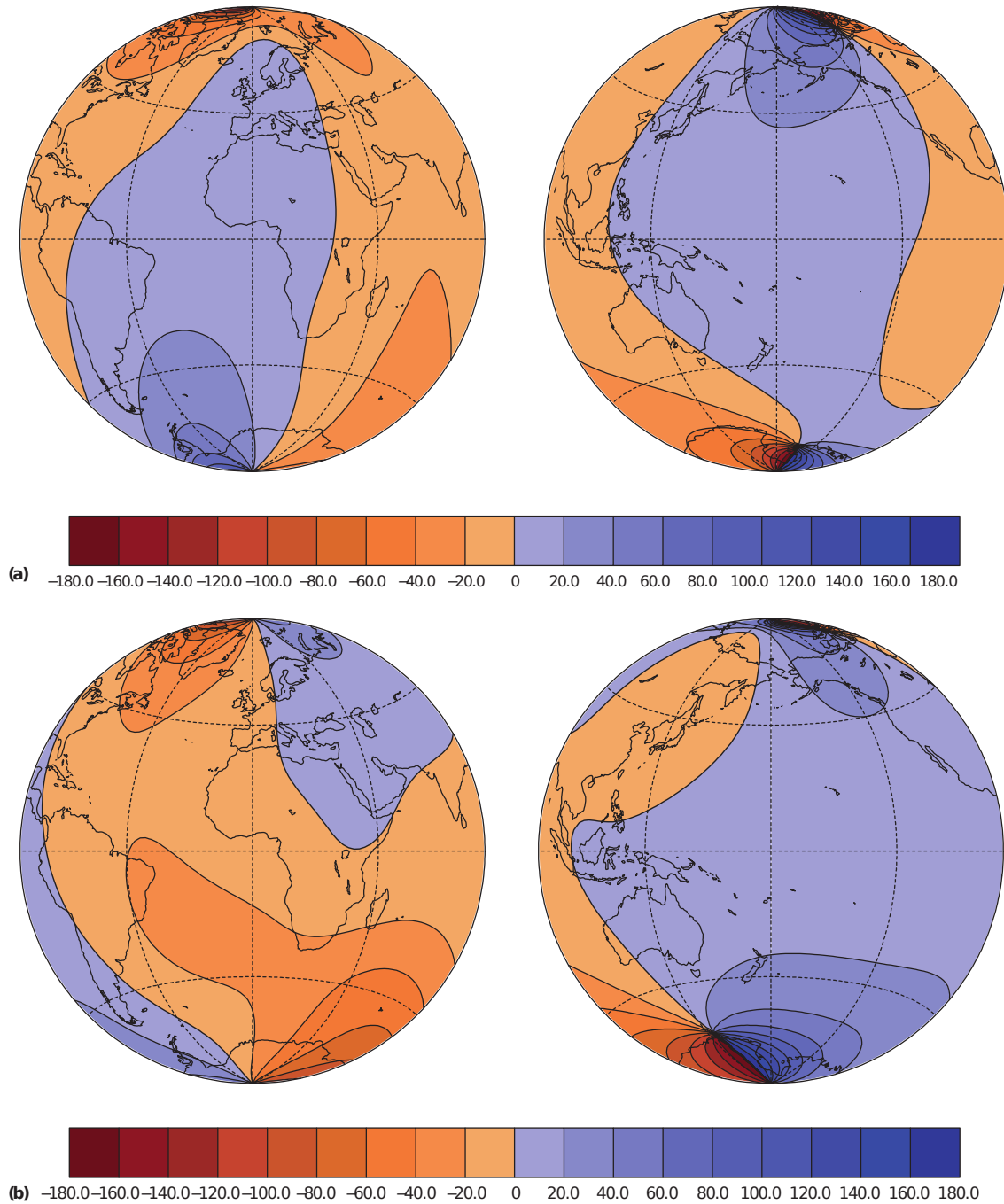


Figure 2.4: A comparison between the magnetic declination at the Earth's surface at the times a) AD 1590 and b) AD 1990. Left pictures show Atlantic hemispheres, right pictures pacific. From Jackson and Finlay (2015).

2010). There are two different types of rock magnetization on Earth: Induced and remanent magnetization, denoted  $\mathbf{M}_i$  and  $\mathbf{M}_r$ , respectively. When a ferromagnetic material is exposed to an ambient magnetic field, it will align itself with the field and gain some magnetization  $\mathbf{M}_i$ , which is the amount of magnetic dipole moment per unit volume with units A/m. The amount of magnetization gained depends on the ambient field ( $\mathbf{H}$ ) and magnetic susceptibility

$k$ , through

$$\mathbf{M}_i = k\mathbf{H} . \quad (2.18)$$

Using the definition of  $\mathbf{H}$

$$\mathbf{H} = \frac{1}{\mu_0}\mathbf{B} - \mathbf{M}_i , \quad (2.19)$$

the magnetic field produced by the magnetization can be written as

$$\mathbf{B} = \mu_0(k + 1)\mathbf{H} . \quad (2.20)$$

The induced magnetization is parallel to the ambient field and serves to strengthen it. Generally, sedimentary rocks have a lower magnetic susceptibility than metamorphic rocks, which in turn have lower susceptibility than igneous rocks.

Remanent magnetization is a permanent alignment of the magnetic moments that has been locked into the material at the time of its formation or when it last underwent a major change. The amount of remanent magnetization is proportional to the ambient field at that time. As such, the remanent magnetization of rock samples can be used to glean information about the core field of the past. The total magnetization of a rock or mineral is the sum of the induced and the remanent magnetization

$$\mathbf{M} = \mathbf{M}_i + \mathbf{M}_r , \quad (2.21)$$

and the relative strength of the two forms of magnetization is called the Königsberger ratio

$$Q = \frac{|\mathbf{M}_r|}{|\mathbf{M}_i|} . \quad (2.22)$$

It is often assumed that  $Q \ll 1$  over the continents and  $Q \gg 1$  in the oceans, meaning that induced magnetization is dominant on land and remanent is at sea.

The lithospheric contribution to the total magnetic field amounts to approximately 3%. The field has a very complex structure covering small scale features of a few kilometres up to geological scales of a couple of thousands of kilometres, depending on the subsurface geology and distribution of ferromagnetic minerals. The crustal field is often assumed to have no temporal variability, as large scale changes in the lithosphere is due to the secular variation of the core field (Thébault et al., 2010).

## 2.3 The external and externally induced fields

Now that the field sources of internal origin are accounted for, we can move on to the external sources, which reside in the iono- and magnetosphere, and the currents they induce in the crust and oceans.

In the ionosphere, the heating of the atmosphere on the dayside and the cooling at the nightside, give rise to a system of tidal winds, which moves ionospheric plasma with it. The movement of this plasma within the core field induces a sheet of electric currents at approximately 110-115 km altitude. These daily geomagnetic variations, known as Sq variations,

have a peak amplitude of 20-50 nT at mid latitudes during magnetically quiet times, and are around twice as large at solar maximum (Olsen, Hulot, & Sabaka, 2014). However, Sq variations only occur on the dayside, so these are normally avoided when modelling the internal field by simply only choosing nightside (dark) data.

The geomagnetic field is strictly horizontal at the magnetic equator, which increases the effective conductivity in the ionosphere, causing a strong eastward current around the equator on the dayside, called the equatorial electrojet. Similarly, there is an auroral electrojet in the polar regions, which can vary from hundreds of nT in geomagnetic quiet times to thousands of nT during geomagnetic storms. This phenomenon is not restricted to the dayside, so these disturbances are more difficult to remove by data selection. There are also some electric fields present at higher altitudes in the ionosphere that cause signals which are detectable in satellites, even on the nightside and in nonpolar regions.

The outer limit of the geomagnetic field is called the magnetopause, and a current runs along this border, producing a long tail in the direction opposite the sun. Within this magnetospheric cavity, the so called neutral sheet currents run in the equatorial plane and the interaction of these currents with the radiation belts produce the ring current that encircles the Earth. There are also streams of electrically charged particles running along the core field lines, these make up the field-aligned currents that couple the ionosphere and the magnetosphere. The field aligned currents are always present, and have amplitudes of up to a hundred nT in quiet times and several thousand nT during geomagnetic storms. There are

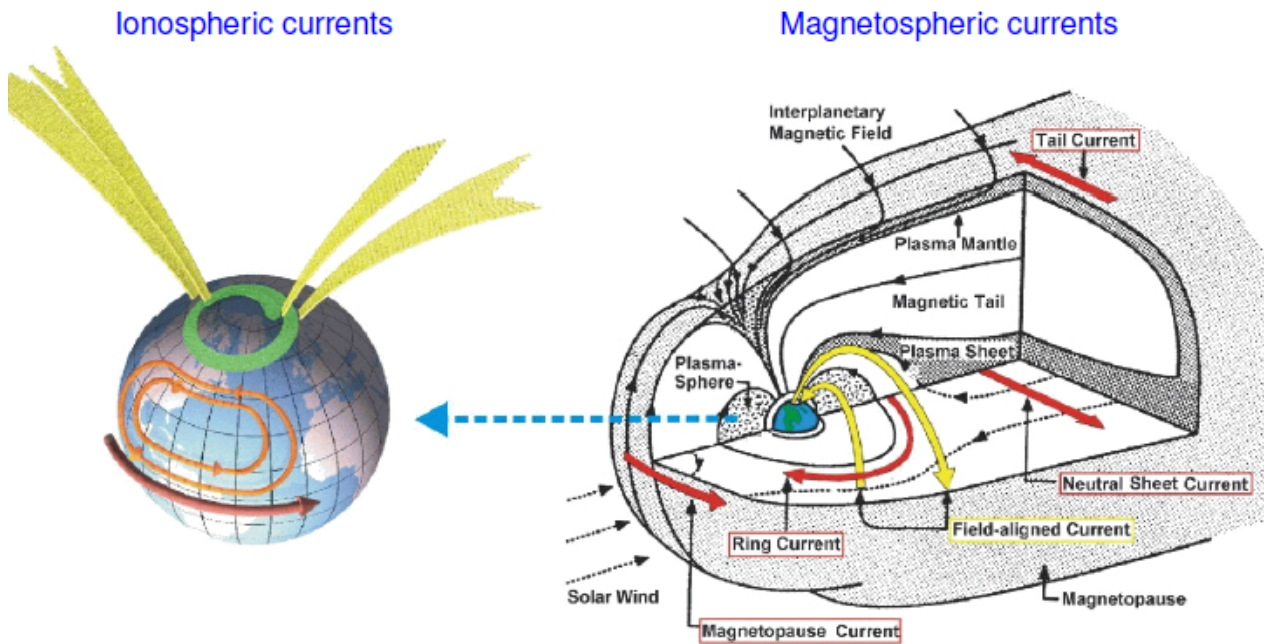


Figure 2.5: An illustration of the sources of the external fields. On the left are shown the ionospheric currents: The Sq variations are shown as orange circles, the equatorial electrojet is indicated by the red arrow, and the green circle represents the auroral electrojet. The yellow arrows are the field aligned currents. On the right the different magnetospheric currents are shown. Taken from Olsen and Finlay (2015).

also currents which couple the Sq variation and the equatorial electrojet to the magnetosphere, but these are smaller and only contribute a few tens of nT at 400 km altitude. All of these different currents are shown schematically in figure 2.5.

The time variation of the external fields induce currents into the Earth’s crust and oceans. The movement of the electrically conducting oceans through the core field also induces currents, in a manner similar to how the movement of the liquid outer core produces currents when it moves through the ambient field. The amplitude of the fields from these induced currents decreases with the scale and the period, as such about one third of the contribution of the Sq variation is due to induced currents, but the induced part of the field due to the equatorial electrojet is much smaller. Even though the oceans contribute to the total field twice, both through externally induced fields and motional induction, the total contribution is rather small and considered negligible at 400 km altitude (Olsen, Hulot, & Sabaka, 2014).

## 2.4 Modelling the geomagnetic field

Having familiarized the reader with the different sources that make up the geomagnetic field, an explanation of how these are currently modelled is in order. The CHAOS series of models (Olsen, Lühr, et al., 2014), currently in its sixth iteration (Finlay et al., 2016), is a good example of the current state of geomagnetic field modelling.

The CHAOS model seeks to determine the magnetic field in Earth-centered Earth-fixed coordinates by way of a scalar potential in two parts

$$V = V_{int} + V_{ext} , \quad (2.23)$$

where  $V_{int}$  describes the internal sources and  $V_{ext}$  describe the external and externally induced sources. This is possible due to the quasi-static approximation: Ampere’s law without displacement current (equation (2.4)) tells us that in regions with no currents, the magnetic vector field can be expressed as the negative gradient of a scalar potential field

$$\mathbf{B} = -\nabla V . \quad (2.24)$$

The fact that the magnetic vector field is divergence free tells us that the scalar potential is a solution to Laplace’s equation

$$\nabla^2 V = 0 , \quad (2.25)$$

the eigenfunctions of which are the spherical harmonics. The scalar potentials are then subjected to a spherical harmonic expansion, the internal part being given by

$$V_{int} = a \sum_{n=1}^{N_{int}} \sum_{m=0}^n (g_n^m \cos m\phi + h_n^m \sin m\phi) \left(\frac{a}{r}\right)^{n+1} P_n^m(\cos \theta) , \quad (2.26)$$

where  $a$  is the radius of the Earth, set to 6371.2 km,  $(r, \theta, \phi)$  are the geographic coordinates,  $P_n^m$  are the associated Schmidt-normalized Legendre functions, the  $g_n^m$  and  $h_n^m$  are Gauss coefficients for the internal sources and  $N_{int}$  is the maximum spherical harmonic degree and order. The external potential contains a spherical harmonic expansion of the magnetospheric

ring-current, and an expansion of the remote sources, such as the tail and magnetopause currents. The former is expressed in solar magnetic coordinates, a coordinate system that has its Z axis parallel to the Earth's magnetic dipole axis, and its Y axis perpendicular to the plane containing the dipole axis and the Earth-sun line. The latter is expressed in Geocentric solar magnetospheric (GSM) coordinates, which has its X axis pointing towards the sun and its Z axis is the projection of the Earth's dipole axis on the plane perpendicular to the X axis. Both are expanded to degree  $n = 2$ , but the term pertaining to remote sources is restricted to  $m = 0$ , resulting in a potential

$$V_{ext} = a \sum_{n=1}^2 \sum_{m=0}^n (q_n^m \cos mT_d + s_n^m \sin mT_d) \left(\frac{r}{a}\right)^n P_n^m(\cos \theta_d) + a \sum_{n=1}^2 q_n^{0,GSM} R_n^0(r, \theta, \phi). \quad (2.27)$$

The Gauss coefficients are now called  $q$  and  $s$ , with  $\theta_d$  and  $T_d$  being the dipole colatitude and local dipole time, respectively. The first degree coefficients of the first term (pertaining to the ring-current) are time-dependent and defined by the RC index, which describes the strength of the magnetospheric ring currents, calculated by spherical harmonic analysis of hourly means from 21 different observatories at mid and low latitudes. The  $q_1^0$  coefficient is given by

$$q_1^0(t) = \hat{q}_1^0 \left[ \epsilon(t) + \iota(t) \left(\frac{a}{r}\right)^3 \right] + \Delta q_1^0(t), \quad (2.28)$$

with the other degree one coefficients being calculated in the same way. The bracketed term is the RC index,  $\hat{q}_1^0$  is a regression coefficient allowing deviations from the RC index value and the  $\Delta q_1^0$  term is a baseline correction. A regularized inversion is performed to find both the internal and external Gauss coefficients, along with the baseline corrections to the RC index, while the regression coefficients are co-estimated.

The final CHAOS model however is the merger of two different sets of model parameters from two different inversions: One for lower spherical harmonic degrees (up to  $n = 80$  for the internal part) and one for higher degrees (up to  $n = 120$  for the internal part). These submodels are referred to as CHAOS-6l and CHAOS-6h, respectively.

The time dependence of the two different models are given by B-splines. Splines are piecewise polynomials, fitted in the intervals between breakpoints, called knots. B-splines are basis functions so that any spline function of some order can be expressed as a linear combination of B-splines of the same order. If we take a sequence of numbers  $\dots < y_{-1} < y_0 < y_1 < \dots$ , the  $m$ th order B-spline  $Q_i^m$  associated with the knots  $y_i, \dots, y_{i+m}$  is then given by

$$Q_i^m(x) = \begin{cases} (-1)^m [y_i, \dots, y_{i+m}] (x - y)_+^{m-1}, & \text{if } y_i < y_{i+m} \\ 0, & \text{otherwise.} \end{cases} \quad (2.29)$$

Here  $(x - y)_+^{m-1}$  is a bit of notation from Schumaker (2007) meaning

$$(x - y)_+^{m-1} = \begin{cases} (x - y)^{m-1}, & x \geq y \\ 0, & \text{otherwise.} \end{cases} \quad (2.30)$$

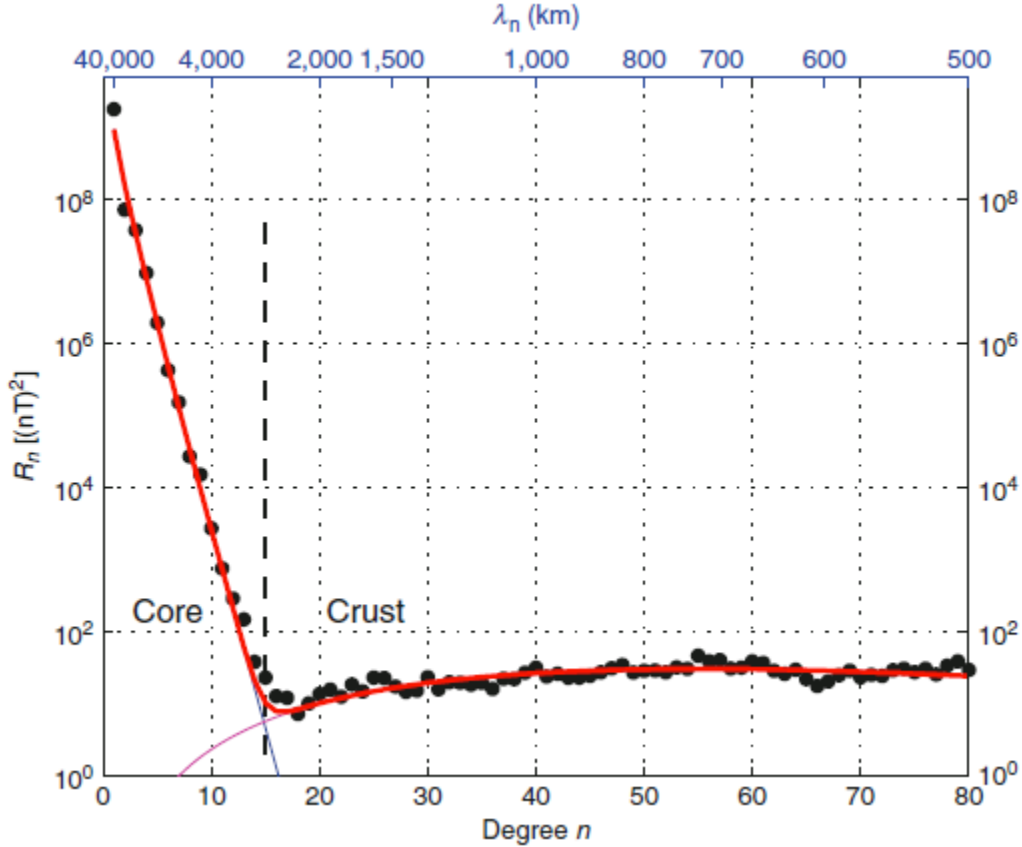


Figure 2.6: Power spectrum of the geomagnetic field at Earth’s surface. The black dots are the power spectrum from recent geomagnetic field models, the magenta line is a theoretical spectrum of the lithosphere, the blue line is a theoretical spectrum of the core and the red line is their superposition. From (Olsen, Hulot, & Sabaka, 2014).

For the low degree model, the Gauss coefficients up to  $n = 20$  are given time dependence by 6th order B-splines with a knot separation of 6 months, the rest of the Gauss coefficients are static. The high degree model uses 3rd order B-splines with the same knots, for coefficients up to degree  $n = 16$ . The reasoning behind using a merger of two submodels is to ensure accurate separation of the core and lithospheric fields. This is usually done by choosing some spherical harmonic degree (often  $n = 14$ ), and then regarding everything at or below this degree as pertaining to the core, and everything above to be caused by the lithosphere. This approach is based on the general appearance of the geomagnetic power spectrum at the Earth’s surface, see figure 2.6. The fact that a superposition of separate theoretical spectra of the core and lithosphere fit the observed spectrum so well suggests that this method is sound. This is also supported by the flatness of the spectrum after degree  $n = 14$ , suggesting that the source of the intensity is close to the surface.

The method of Finlay et al. (2016) is however more sophisticated than a simple truncation: The low degree model has been determined using a full dataset consisting of ground observatory measurements as well as satellite data from Ørsted, CHAMP, SAC-C and Swarm spanning a period from January 1997 to March 2016. The high degree model utilizes only

late CHAMP data, when the satellite orbit had a lower altitude, as this is optimal for sampling the lithospheric field. The final CHAOS-6 model then consists of the Gauss coefficients from CHAOS-6l, replacing the static field Gauss coefficients of degree higher than 24 with the same coefficients from CHAOS-6h. The cut of point is  $n = 24$  because the degree correlation between the two models reach a maximum at this point while the relative difference is less than 0.2% (Olsen, Lühr, et al., 2014). The result is a comprehensive model of the geomagnetic field that can represent both internal and external sources, as well as separate the core and lithospheric fields.

There are of course many other different time dependent models of the geomagnetic field to chose from, but the vast majority of them employ similar methods: A spherical harmonic expansion of the field in terms of Gauss coefficients, and most models since the mid 1980s utilize B-splines to model the time dependence. There are different reasons to this convergence in modelling technique. The choice of using spherical harmonics is apparent from the fact that they are eigenfunctions to Laplace’s equation, but they are also convenient in the way that the maximum spherical harmonic degree immediately gives the complexity of a model, and from the way that the models can be compared and analysed using the spherical harmonic power spectrum. Separation of internal and external sources, as well as up- and downward continuation of the field is also handled nicely by spherical harmonics.

Spherical harmonics also have their limitations however. The global nature of the Gauss coefficients makes it difficult to model regional features, which is problematic when modelling the crustal field, as the number of data and representing functions increase with the inverse square of the spatial wavelength, making global modelling of short scale phenomenon cumbersome. This can be remedied by regional modelling, but since spherical harmonics as sources are centred at the origin, dense sampling of regional data can appear like lower order spherical harmonics, causing ill-conditioning (O’Brien & Parker, 1994).

The reasoning behind B-splines being the temporal basis of choice is twofold: They are local, meaning that the basis functions are zero outside of small range, and this sparsity is advantageous with regards to storage and computation time. Secondly, they are by their nature smooth and continuous, which is desirably because the amount of spurious detail in any model should be minimized. This smoothness can however also be an inconvenience, as models based on B-splines can have problems in capture the fast changes in the small scale field, such as geomagnetic jerks (Jackson & Finlay, 2015).

In the present thesis, we will set out to address these issues, by implementing an analogous spatial representation based on an equal area distribution of monopoles on the surface of a sphere, located within the Earth’s core. This approach is very flexible, and should be able to accurately model features on any scale. It is our ambition that the monopole representation, together with an L1-norm regularization of the radial field at the core surface, will allow us to represent sparse features at core-mantle boundary that would normally be smoothed out by a conventional model based on spherical harmonics. Instead of modelling the time-dependence with B-splines, we will adopt a more flexible approach based on temporal covariance functions. The right choice of function and its associated hyperparameters will allow us to model a more “rough” time-dependence than B-splines, which should enable us to capture the geomagnetic jerks better in our model. The modelling scheme, as well as the implementation of the regularization, is explained in detail in chapter 4.

# Chapter 3

## Measurements and data selection

Before we get to the modelling scheme in chapter 4, this chapter will provide descriptions of the different data sets used for the inversion, as well as the selection criteria used to ensure the quality of the measurements. Three different types of data are used in this thesis:

- Measurements of the secular variation of the three different magnetic field components ( $r$ ,  $\theta$  and  $\phi$ ) made by a number of ground-based observatories scattered across the Earth, covering a time period of 1998 to 2016.
- Measurements of the  $r$ -component of the magnetic main field made by the German CHAMP satellite from ca. 2000-2010.
- Measurements of the  $r$ -component of the magnetic main field made by ESA's Swarm satellite trio from ca. 2014-2016.

Ground and satellite based measurements are fundamentally different and therefore good at performing different tasks. Advantages of the ground observatories are that the data is much less subjected to noise than satellite measurements, as satellites are affected by space weather and other atmospheric disturbances. Another advantage is that the static nature of the observatories allow for accurate measurements of the secular variation of the magnetic field, which is difficult for satellites since they move with high velocities, so it can be hard to determine whether a magnetic field variation is due to a spatial or temporal change.

The main advantage of satellite measurements is of course the near global coverage that they provide, and the fact that the same measurement apparatus is used over different regions, which minimizes discrepancies that could be caused by comparing measurements from different equipment (Olsen et al., 2010).

### 3.1 Ground observatories

The ground observatory dataset used has been provided by INTERMAGNET, the International Real-time Magnetic Observatory Network, which is a global network of cooperating digital magnetic observatories with modern technical standards, that provide high quality magnetic measurements in close to real time. The observatories measure the local variations

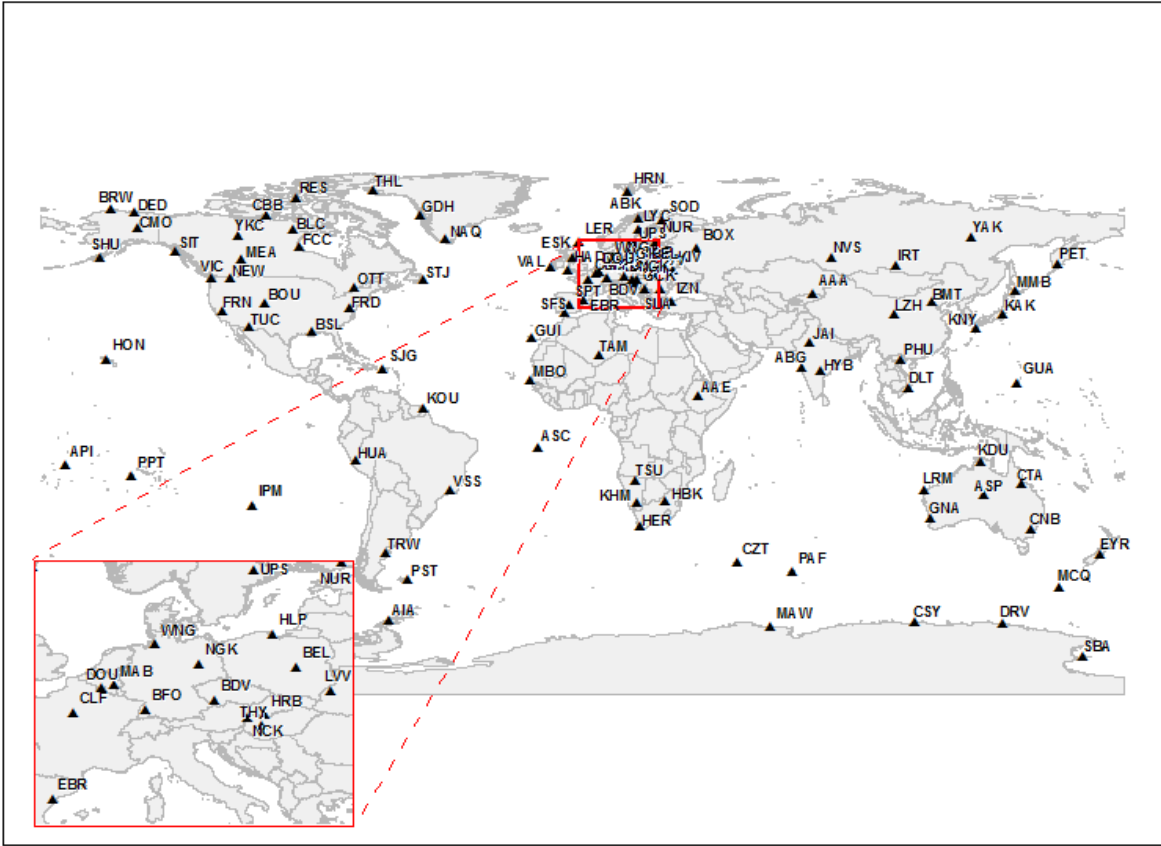


Figure 3.1: Map showing the locations of the geomagnetic observatories that make up INTERMAGNET.

in the three magnetic field components with a vector magnetometer, where any contamination from man-made interference and faulty equipment is removed. This variation is then combined with a baseline measurement made with an absolute magnetometer to give the actual value of the main field (Matzka et al., 2010). These measurements are then collected in so-called revised monthly mean (RMM) values, and the secular variation (SV) is calculated by subtracting data one year apart, for example

$$SV = RMM_j - RMM_i \quad (3.1)$$

Where  $i$  is some point in time and  $j = i + 1\text{yr}$ . This is performed for all three components of the magnetic field. In total, measurements from 174 different observatories scattered all across the globe are used, however the density of observatories is larger in the northern hemisphere, particularly in Europe, see figure 3.1.

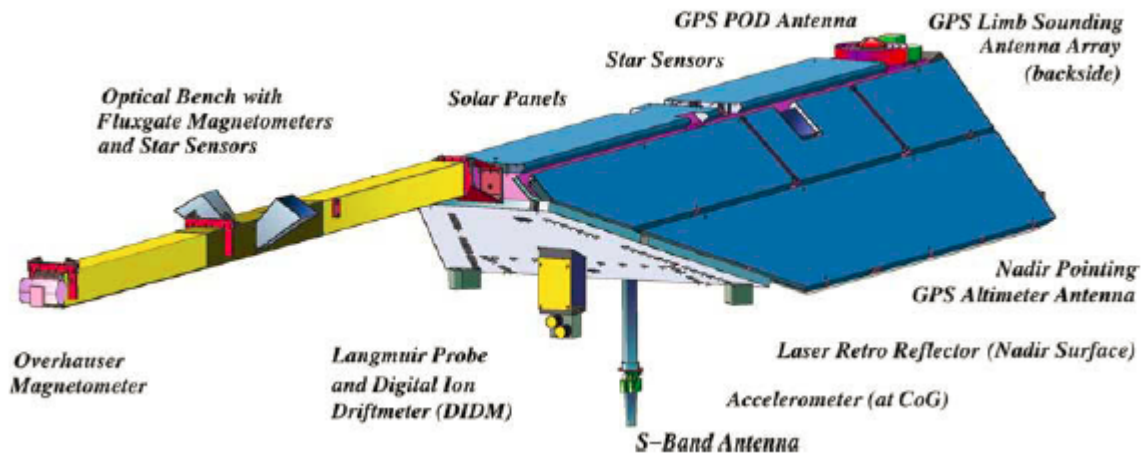


Figure 3.2: Sketch showing the CHAMP satellite and the placements of the different instruments. From Maus (2007).

## 3.2 The CHAMP satellite

CHAMP (CHALLENGING Minisatellite Payload) was a small German satellite used for geoscientific measurements. CHAMP was launched from Plesetsk in Russia, on July 15, 2000, into a near-circular, near-polar orbit with an initial altitude of 454 km. The mission was intended to last 5 years, but ended up lasting for 10 years and 2 months, when it ended on September 19, 2010. CHAMP contained a diverse array of instruments for precision measurements of the magnetic and gravitational field. To ensure that the magnetic measurements were uncontaminated by electrical interference from the rest of the satellite, all of the magnetometry assembly was fitted to a boom that protrudes 4 meters out from the front end of the satellite.

The assembly consisted of two redundant vector magnetometers, a scalar magnetometer, a star camera, a digital ion drift meter (DIDM) and a planar Langmuir probe (PLP). The scalar magnetometer was placed at the end of the boom, and measured the total intensity of the magnetic field every second with an accuracy of  $< 0.5$  nT. These measurements were used to calibrate the vector magnetometers, which were fixed to an optical bench around the midpoint of the boom. These fluxgate vector magnetometers were developed at DTU Lyngby and sampled the magnetic field with a frequency of 50 Hz and a resolution of  $< 0.1$  nT. In order to get correct vector measurements, precise determination of the satellite attitude is required. This was achieved by the use of a dual head star camera fitted to the optical bench, also developed at DTU Lyngby. The DIDM was supposed to measure the velocities of ions and the strength of any electric field surrounding the spacecraft, but this apparatus failed during launch. The PLP measures the spacecraft potential along with the electron temperature and density, which are quantities that are needed to correct the magnetic field measurements from the influence of any plasma surrounding the satellite. See figure 3.2 for an illustration of the satellite.

The CHAMP mission served to improve upon the models of the main field and the secular variation already obtained through previous satellites such as Ørsted. The orbital characteristics of the CHAMP satellite meant that it was particularly suited for mapping the

crustal field, and even a signal corresponding to the magnetic field produced by the periodic ocean flow was identified (Maus, 2007).

### 3.3 The Swarm satellite trio

In November 2013, ESA’s Swarm satellite constellation was launched to provide the most accurate measurements of the Earth’s magnetic field to date. The constellation is composed of three different satellites (Swarm A, B and C), which are structurally very similar to the CHAMP satellite, consisting of a compact frame with a 4 m long boom, and a magnetometry assembly similar to CHAMPS, with some improvements in measurement accuracy. The absolute magnetometer has an accuracy of 0.3 nT, and the star cameras on Swarm have three heads instead of two, further improving the attitude determination. As with CHAMP, the Swarm satellites also contain instruments to measure the surrounding electric fields and plasma densities, which is needed to correct the measurements.

The main difference between the CHAMP and Swarm missions is the fact that Swarm is a constellation of three separate satellites, instead of a single one. The three satellites carry identical instrumentation, making direct comparison between measurements of the different satellites possible. As mentioned previously, one of the major drawbacks of satellite observations are that it can be difficult to determine whether variations are of a spatial or temporal nature. This problem is remedied by Swarm, as measurements from different locations at the same time can be directly compared. The orbital characteristics of the three satellites have been designed so that the external and internal sources can be separated, as well as the lithospheric and core fields. Satellites A and C fly side-by-side decaying naturally from an orbit of 460 km to 300 km, while satellite B orbits above them at 530 km, with a slightly different inclination. This inclination changes with time, resulting in a 90° angle between the upper satellite and the lower ones after 3 years of operation (Friis-Christensen et al., 2006).

### 3.4 Satellite data selection criteria

The amounts of data collected by CHAMP and Swarm are very large, so careful data selection has been performed both to reduce the amount of data used and to make sure that the data is of high quality. A basic sampling rate of 10 minutes has been chosen, and only data from dark regions at geomagnetically quiet times have been used. A dark region has the sun at an angle of 10° or lower below the horizon, and geomagnetic quiet times are defined as having:

- $K_p$  index equal to or less than 2
- Change in RC index equal to or less than 2 nT/hr
- $E_m$  averaged over the last 2 hours equal to or less than 0.8 mV/m
- Interplanetary magnetic field (IMF)  $B_z$  averaged over proceeding two hours  $\geq 0$

The  $K_p$  index is a global index characterising the level of geomagnetic activity, 0 being completely quiet and 9 being severe geomagnetic storming. The index is calculated as the

weighted average of individual K-indices, which are logarithmic indices calculated by the maximum fluctuations of the horizontal component of observatory magnetometer readings, adjusted for geomagnetic latitude. The RC index describes the strength of the magnetospheric ring current.  $E_m$  is the merging electric field at the magnetopause, defined as

$$E_m = vB_t \sin^2(\Theta/2) \quad (3.2)$$

where  $v$  is the solar wind speed,  $B_t = \sqrt{B_y^2 + B_z^2}$  is the interplanetary magnetic field in the y-z plane in geocentric solar magnetospheric coordinates, and  $\Theta = \arctan(B_y/B_z)$ . The reasoning behind the final selection criteria, is that disturbances related to the auroral electrojet are especially prominent when IMF  $B_z < 0$ .

The same data selection criteria have also been used to derive the CHAOS-6 models (Finlay et al., 2016). The data sets have received further treatment with help from the CHAOS-6 model: All points with values that are more than 100 nT different from CHAOS-6 model estimates have been removed, and CHAOS-6 estimates of the static crustal field and external magnetospheric fields have also been removed, in order to isolate the core field.

# Chapter 4

## Method

This section contains a detailed explanation of the model parametrization and inversion techniques used in this thesis. As mentioned in section 2.4, a monopole representation of the core field will be applied, and time-dependence will be modelled using covariance functions. Firstly, the forward problem is described and we derive the design matrices that map the monopole amplitudes to magnetic field values at the core surface. Then follows an explanation of how these design matrices are used to invert for the model parameters, i.e. the monopole amplitudes.

### 4.1 The monopole forward modelling scheme

The Earth's core magnetic field is modelled as the field resulting from the individual contributions of a spherical grid of magnetic monopoles placed inside the Earth's core, each of which has some magnetization  $\pm m$ . Following the approach of O'Brien and Parker (1994), which has also been implemented by Kother et al. (2015), we begin with a set of measurements of the magnetic field components  $d_i$ ,  $i = 1, \dots, N$  at some points  $\mathbf{r}_i(r_i, \theta_i, \phi_i)$ . The resulting potential field  $\Phi$  at position  $\mathbf{r}_i$  due to a collection of magnetic monopoles at positions  $\mathbf{r}_j(r_j, \theta_j, \phi_j)$  and each contributing a potential  $\phi_j(\mathbf{r}_i)$ ,  $j = 1, \dots, M$  is then given by

$$\Phi(\mathbf{r}_i) = \sum_{j=1}^K m_j \phi_j(\mathbf{r}_i) . \quad (4.1)$$

Assuming here that  $M < N$  and that the  $\phi_j(\mathbf{r}_i)$  are linearly independent, the relationship between the potential and the measurements can be expressed in source-free regions as

$$d_i = - \sum_{j=1}^K m_j \cdot \nabla \phi_j(\mathbf{r}_i) \quad (4.2)$$

$$d_i = \sum_{j=1}^K m_j g_{ij} . \quad (4.3)$$

This can be written in matrix form as

$$\mathbf{d} = \underline{\underline{\mathbf{G}}}\mathbf{m} , \quad (4.4)$$

where  $\mathbf{d}$  is a vector of the measured data,  $\underline{\underline{\mathbf{G}}}$  is an  $N \times M$  design matrix which relates the monopole functions  $\phi_j(\mathbf{r}_i)$  to the measurements. These monopole potential functions are very simple. They are given by the distance between the position vectors of the measurement points and the monopole locations

$$\phi_j(\mathbf{r}_i) = \frac{1}{|\mathbf{r}_i - \mathbf{r}_j|} , \quad (4.5)$$

where  $|\mathbf{r}_i - \mathbf{r}_j|$  is given by

$$|\mathbf{r}_i - \mathbf{r}_j| = \sqrt{\mathbf{r}_i^2 + \mathbf{r}_j^2 - 2\mathbf{r}_i\mathbf{r}_j \cos \mu_{ij}} . \quad (4.6)$$

Here,  $\mu_{ij}$  is the angle between the two position vectors given by

$$\cos \mu_{ij} = \cos \theta_i \cos \theta_j + \sin \theta_i \sin \theta_j \cos(\phi_i - \phi_j) . \quad (4.7)$$

The design matrix is then calculated by taking partial derivatives of equation 4.5 for the three different components

$$\underline{\underline{\mathbf{G}}}_r(\mathbf{r}_i) = -\frac{\partial}{\partial r_i} \left( \frac{1}{|\mathbf{r}_i - \mathbf{r}_j|} \right) \quad (4.8)$$

$$\underline{\underline{\mathbf{G}}}_\theta(\mathbf{r}_i) = -\frac{1}{r_i} \frac{\partial}{\partial \theta_i} \left( \frac{1}{|\mathbf{r}_i - \mathbf{r}_j|} \right) \quad (4.9)$$

$$\underline{\underline{\mathbf{G}}}_\phi(\mathbf{r}_i) = -\frac{1}{r_i \sin \theta_i} \frac{\partial}{\partial \phi_i} \left( \frac{1}{|\mathbf{r}_i - \mathbf{r}_j|} \right) , \quad (4.10)$$

which then gives

$$\underline{\underline{\mathbf{G}}}_r(\mathbf{r}_i) = \frac{r_i - r_j \cos \mu_{ij}}{|\mathbf{r}_i - \mathbf{r}_j|^3} \quad (4.11)$$

$$\underline{\underline{\mathbf{G}}}_\theta(\mathbf{r}_i) = \frac{r_j (\cos \theta_j \sin \theta_i - \cos(\phi_i - \phi_j) \cos \theta_i \sin \theta_j)}{|\mathbf{r}_i - \mathbf{r}_j|^3} \quad (4.12)$$

$$\underline{\underline{\mathbf{G}}}_\phi(\mathbf{r}_i) = \frac{r_j \sin(\phi_i - \phi_j) \sin \theta_j}{|\mathbf{r}_i - \mathbf{r}_j|^3} . \quad (4.13)$$

These three components can then be combined to construct the full design matrix. The  $\underline{\underline{\mathbf{G}}}$  matrix only depends on the locations of the measurements and the monopoles, and since the measurement locations are fixed by the data, the design matrix depends entirely upon how the monopoles are distributed within the Earth's core.

## 4.2 Distribution of points on a sphere and integrating on the sphere

In order to build the necessary design matrices for the inversion, two different ways of distributing points on a sphere are needed. One very flexible method, called recursive zonal equal area sphere partitioning, is used to create a grid of monopoles. Another method based upon Lebedev quadrature is convenient and efficient for solving integrals on the surface of a sphere, which becomes necessary when inverting for a large (and sparse) model. The following section is a short description of these two methods and their implementation.

### 4.2.1 Recursive zonal equal area sphere partitioning

The  $M$  individual monopoles which make up the magnetic field should be equally distributed on the surface of a sphere of some radius smaller than the core radius  $c = 3480$  km. To this end, the recursive zonal equal area sphere partitioning algorithm developed by Leopardi (2006) is used. The inputs are the desired dimension and number of partitions. The algorithm then partitions the unit sphere of the given dimension  $D$  into  $M$  regions of equal area and small diameter, and outputs the cartesian coordinates of the midpoints of these regions. A short step-by-step description of how the algorithm works follows, see figure 4.1 for a visual description for the case  $D = 3$ ,  $M = 99$ .

The sphere is first divided into zones, each the same area as an integer number of regions.

1. **Determine the colatitudes of polar caps.** A polar cap is a spherical cap centred at one of the poles, with the same area as that required for a region.
2. **Determine an ideal collar angle.** A collar is a horizontal band across the unit sphere, defined as the difference between two spherical caps with the same midpoint but different radii. The ideal collar angle is defined as the polar cap area to the power of  $1/3$ , using here that the spherical distance is approximately equal to the Euclidean for small distances.
3. **Determine the ideal number of collars.** This is done by finding how many collars with the ideal collar angle can fit onto the unit sphere with the north and south polar caps also in place.
4. **Determine the actual number of collars.** This is simply done by rounding the ideal number, in order to get integer values.
5. **Create a list of the ideal number of regions in each collar.** The zones are all given numbers, and the ideal number of regions in each collar is calculated as the area of a collar divided by the area of a region (which is equal to area of one of the polar caps).
6. **Create a list of the actual number of regions in each collar.** This is once again done by a rounding to get integer values.
7. **Create a list of colatitudes of each zone.** The colatitude of each zone is calculated, as these values along with the actual number of regions in each collar are needed for the final step.

When the lists from step 6 and 7 have been created, the same algorithm is then run on each collar, where the input is now the chosen dimension  $D - 1$  with number of regions being equal to the actual number of regions for the given collar.

From this algorithm, the Cartesian coordinates for  $M$  monopoles approximately equal area distributed on the unit sphere is obtained. These are then converted to spherical coordinates and allocated some radius smaller than the core radius, in order to specify the monopole grid. The  $\underline{\underline{\mathbf{G}}}$  matrix can then be computed from the coordinates of the monopoles and the measurements.

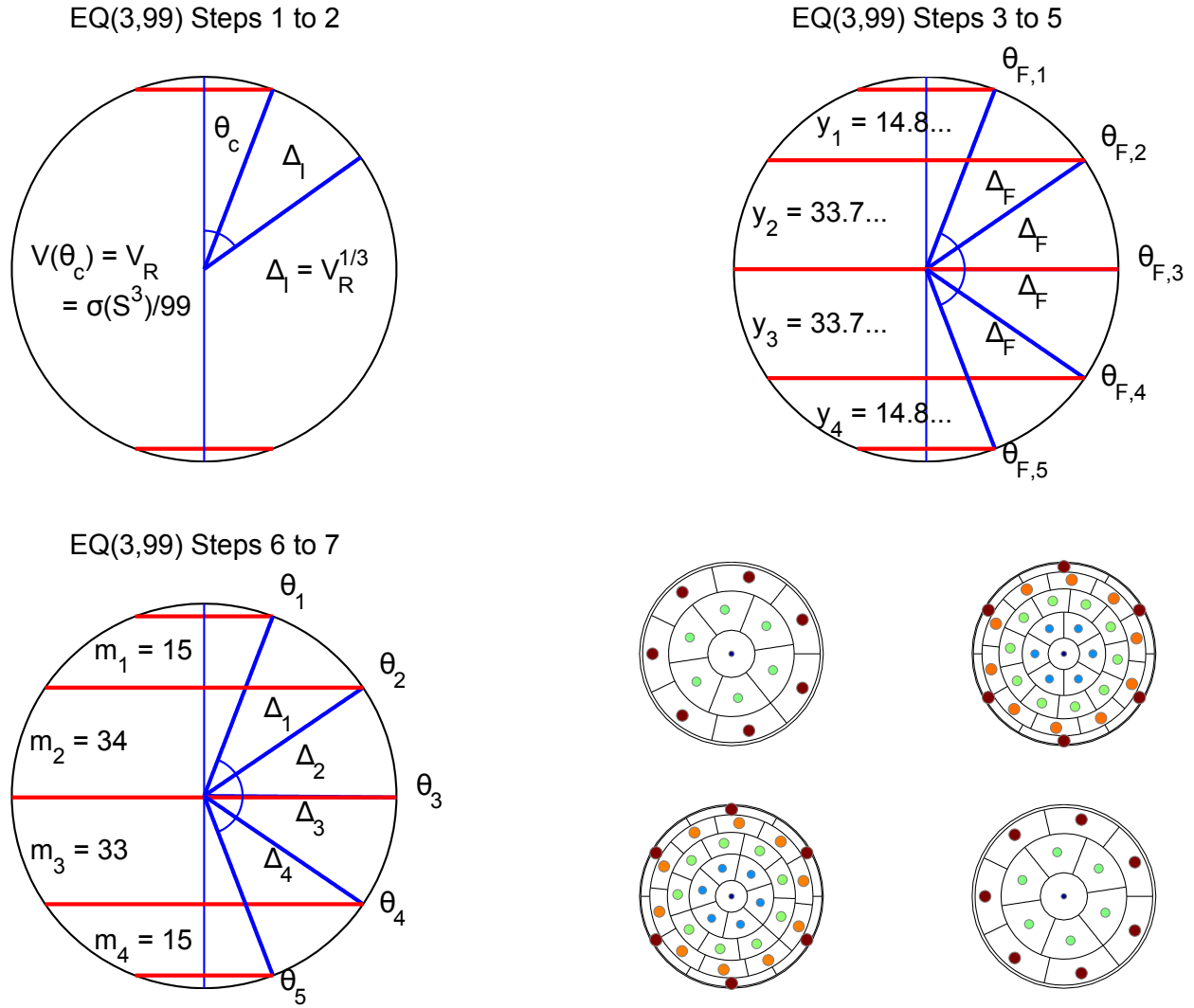


Figure 4.1: Illustration of the algorithm for 3 dimensions and 99 points. In top left, the colatitude of the polar cap ( $\theta_c$ ) and the ideal collar angle is found ( $\Delta_i$ ).  $V(\theta_c) = V_R$  is the area of a region. In the top right, the angles for the actual (as opposed to the ideal) collars are found ( $\Delta_F$ ), with  $\theta_{F,i}$  as their colatitudes. The numbers  $y$  are the ideal number of regions in each collar. In the bottom left, the regions and colatitudes are listed, with  $m$  being the actual (rounded) number of regions in each collar. In the bottom right, the same algorithm is used to divide the collars into regions. From Leopardi (2006).

$N_l$	6	14	26	38	50	74	86	110	146	170	...	5810
$L$	3	5	7	9	11	13	15	17	19	21	...	131

Table 4.1: Table of the Lebedev rules, showing the number of points on the spherical surface ( $N_l$ ) and the spherical harmonic degree ( $L$ ) and order they can be used to integrate up to.

## 4.2.2 Lebedev Quadrature

During the solution of the inverse problem, we will need to minimize a norm of the radial magnetic field at the core surface, which requires the solving of integrals on a spherical surface of the form

$$\int f(\Omega)d\Omega = \int_0^{2\pi} \int_0^\pi f(\theta, \phi) \sin(\theta)d\theta d\phi , \quad (4.14)$$

in order to get the unsigned flux. A very efficient way of evaluating such integrals was developed by Lebedev and Laikov (1999), by considering a set of points on the unit sphere which are invariant under the octahedral rotation group with inversion. Laikov developed an algorithm that gives the coordinates of a set of points on the unit sphere  $\mathbf{r}_k$ ,  $k = 1, \dots, N_l$ , along with some associated weights  $w_l$ , so the integral over spherical harmonics can be evaluated as a sum

$$\int f(\Omega)d\Omega = \sum_{k=1}^{N_l} w_l f(\mathbf{r}_k) . \quad (4.15)$$

The algorithm only allows some particular numbers of points called rules ( $N_l$ ), each of which can solve the integral up to some maximum spherical harmonic degree and order ( $L$ ), to within an accuracy of  $10^{-14}$ , see table 4.1. This can be done all the way up to a grid of 5810 points, corresponding to spherical harmonic degree and order 131. In practice, the algorithm is run to get the Cartesian coordinates of the  $N_l$  Lebedev points and their associated weights ( $\mathbf{w}_l$ ), the Cartesian coordinates are then converted to spherical coordinates. The spherical grid is given a radius equal to the core radius, which is where we wish to perform the integration. A design matrix ( $\underline{\underline{\mathbf{G}}}_l$ ) is then calculated from the radial derivatives of the inverse distance vectors between the monopole grid points and the Lebedev grid points, in order to calculate predictions of a monopole model for the radial field  $B_r$  at the Lebedev points  $N_l$ . This design matrix and the Lebedev weights can then be used to evaluate integrals over the surface of the Earth's core (S), as an example, the flux of  $B_r$  would be

$$\int_S \mathbf{B}_r dS = \mathbf{w}_l^T \underline{\underline{\mathbf{G}}}_l \mathbf{m} , \quad (4.16)$$

with  $\mathbf{m}$  being a vector of the monopole amplitudes.

## 4.3 Modelling time dependence using temporal covariance functions

The forward modelling scheme described in the preceding sections is static: Each monopole has a fixed amplitude and the resulting magnetic field is therefore static. We now allow the

monopole amplitudes to change with time, introducing this time dependence using temporal covariance functions, a method described by Rasmussen and Williams (2006). In this approach, the change in amplitude for a given monopole between two points in time  $t_1$  and  $t_2$  is specified using the covariance between these two times, as calculated by a chosen covariance function  $k$ , depending on a number hyperparameters. An example of such a covariance function is the squared exponential

$$k_{SE}(t_1, t_2) = \sigma_f^2 \exp\left(-\frac{1}{2} \frac{|t_1 - t_2|^2}{\tau^2}\right). \quad (4.17)$$

Here  $\sigma_f^2$ , the expected signal variance, is a hyperparameter determining the amplitude of the signal variations and  $\tau$  is a hyperparameter defining a characteristic time scale, which can be thought of as the amount of time that must pass for a significant change in function value to occur.

The squared exponential covariance function generally results in very smooth time-dependence, which isn't suitable if we want to model rapid change events, such as geomagnetic jerks. In order to account for such events, one can instead choose a different covariance function, for example from the more flexible Matérn class. This form of covariance function takes an additional hyperparameter called  $\nu$ , which determines how 'rough' the time-dependence is. In our application, it can only take the values 1, 3 or 5, with 1 allowing very fast change and 5 being smoother and more akin to the results obtained by a squared exponential function. The Matérn function for the three different values of  $\nu$  is given by

$$k_{\nu=1}(t_1, t_2) = \sigma_f^2 \exp\left(-\frac{|t_1 - t_2|}{\tau}\right) \quad (4.18)$$

$$k_{\nu=3}(t_1, t_2) = \sigma_f^2 \left(1 + \frac{\sqrt{3}|t_1 - t_2|}{\tau}\right) \exp\left(-\frac{\sqrt{3}|t_1 - t_2|}{\tau}\right) \quad (4.19)$$

$$k_{\nu=5}(t_1, t_2) = \sigma_f^2 \left(1 + \frac{\sqrt{5}|t_1 - t_2|}{\tau} + \frac{5|t_1 - t_2|^2}{3\tau^2}\right) \exp\left(-\frac{\sqrt{5}|t_1 - t_2|}{\tau}\right). \quad (4.20)$$

A previous study by Gillet et al. (2013) has shown that a Matérn covariance function with  $\nu = 3$  describes the secular variation at ground observatories well, further motivating its use, and the simpler squared exponential will be used for comparison. Many other choices of covariance function are available, but only these two are investigated here.

### 4.3.1 A time-dependent design matrix

In practice, model time-dependence is implemented by calculating a covariance matrix whose entries  $\underline{\underline{\mathbf{K}}}(i, j)$  are given by the covariance function  $k(t_i, t_j)$ , between a set of magnetic data points  $t_i$ ,  $i = 1, \dots, N$ , and a set of reference points  $t_j$ ,  $j = 1, \dots, R$ , at which we choose to evaluate the monopole amplitudes. This  $N \times R$  covariance matrix  $\underline{\underline{\mathbf{K}}}$  serves as a temporal design matrix, which is combined with the  $N \times M$  spatial design matrix  $\underline{\underline{\mathbf{G}}}$ , relating the monopole amplitudes to magnetic field observations, in order to carry out a time-dependent inversion.

This combination is done as follows: The spatial design matrix  $\underline{\underline{\mathbf{G}}}$  is horizontally concatenated  $R$  times, resulting in a new matrix  $\underline{\underline{\mathbf{G}}}^{spatial}$  with dimensions  $N \times P$ ,  $P = M \cdot R$ . The columns of  $\underline{\underline{\mathbf{K}}}$  are each repeated  $M$  times, producing an  $N \times P$  matrix of the time dependence  $\underline{\underline{\mathbf{K}}}^{temporal}$ , which can then be multiplied with  $\underline{\underline{\mathbf{G}}}^{spatial}$  element-wise in order to produce the final time dependent design matrix

$$\underline{\underline{\mathbf{G}}}(i, j) = \underline{\underline{\mathbf{G}}}^{spatial}(i, j) \cdot \underline{\underline{\mathbf{K}}}^{temporal}(i, j) , \quad (4.21)$$

see algorithm 1 for a pseudocode explanation of the process. A regularized inversion (see section 4.4) can then be performed, resulting in a vector  $\mathbf{m}$  of  $P$  magnetic monopole amplitudes at each of the  $R$  different reference times. Once such a vector of amplitudes has been created, it can be used for making predictions by constructing a new design matrix for the points and times where magnetic field predictions are required. The covariance matrix is built the same way, but instead of  $t_i$  being the times of data measurements, they are now chosen to be the times where magnetic field predictions are needed

$$\mathbf{d}_{pred} = \underline{\underline{\mathbf{G}}}\mathbf{m} . \quad (4.22)$$

---

**Algorithm 1** Pseudocode showing the process of calculating a time-dependant design matrix for the radial field component.  $N$  is the number of data points,  $R$  is the number of reference times,  $\cos \mu$  is as in equation (4.7) and  $dist$  is as  $|\mathbf{r}_i - \mathbf{r}_j|$  in equation (4.6), where  $\theta_m$  are the co-latitudes of the monopoles and  $\theta_d(i)$  is the co-latitude of the  $i$ 'th data point, which is the same notation used for the longitudes  $\phi_d, \phi_m$  and radial coordinates  $r_d, r_m$ .

---

**for**  $i=1:N$  **do**

$$\cos \mu = \cos \theta_d(i) \cos \theta_m + \sin \theta_d(i) \sin \theta_m \cos(\phi_d(i) - \phi_m)$$

$$dist = \sqrt{\mathbf{r}_d(i)^2 + \mathbf{r}_m^2 - 2\mathbf{r}_d(i)\mathbf{r}_m \cos \mu}$$

$$\underline{\underline{\mathbf{G}}}^{spatial}(i) = (r_d(i) - r_m \cos \mu) / dist^3$$

**end for**

$$\underline{\underline{\mathbf{G}}}^{spatial} = repmat(\underline{\underline{\mathbf{G}}}^{spatial}, 1, R)$$

$$\underline{\underline{\mathbf{G}}}^{time}(i, j) = \underline{\underline{\mathbf{G}}}^{spatial}(i, j) \cdot \underline{\underline{\mathbf{K}}}^{temporal}(i, j)$$


---

### 4.3.2 Modelling the secular variation.

As mentioned in section 3, the observatory data sets do not consists of measurements of the main field components, but of the secular variation, calculated as the difference of two monthly means one year apart. A design matrix that relates monopole values to the secular variation observations is therefore necessary to perform an inversion with secular variation data. The approach in doing this is rather straight forward: Calculate two time-dependent design matrices as in the previous section, one for some time  $i$  and one for  $j = i + 1\text{yr}$  and calculate the difference of the two

$$\underline{\underline{\mathbf{G}}}^{SV} = \underline{\underline{\mathbf{G}}}_j - \underline{\underline{\mathbf{G}}}_i . \quad (4.23)$$

## 4.4 Solving the inverse problem

Having derived the necessary design matrices, we are now ready to perform the inversion. Two different inversions will be performed: One using an L2 regularization of the model parameters, and one which is made by minimizing the L1 norm of the radial magnetic field at the core surface.

### 4.4.1 L2 regularized inversion

Determining the physical characteristics of the Earth's magnetic field from the amplitudes of the individual monopoles on a chosen grid is regarded as the forward problem. The inverse problem is to find the monopole amplitudes from measurements of the Earth's magnetic field. To solve the inverse problem, an iteratively re-weighted least squares (IRLS) method involving Huber weights in the misfit function is used. The IRLS approach helps to ensure a robust solution, meaning that the solution is not sensitive to large outliers in the data. The solution is also regularized to ensure stability when evaluating the field at the core surface.

This is achieved by minimizing an objective function consisting of a series of norms chosen on the basis of some assumptions concerning the desired properties of the model. The first and most obvious quantity to minimize is a norm of the data misfit  $E(\mathbf{m})$ , defined as the difference between measured and predicted magnetic field intensities

$$E(\mathbf{m}) = (\mathbf{d} - \underline{\underline{\mathbf{G}}}\mathbf{m})^T \underline{\underline{\mathbf{W}}}(\mathbf{d} - \underline{\underline{\mathbf{G}}}\mathbf{m}) . \quad (4.24)$$

Here  $\mathbf{d}$  is the observed data,  $\underline{\underline{\mathbf{G}}}$  is the design matrix and  $\mathbf{m}$  is a vector of the monopole amplitudes.  $\underline{\underline{\mathbf{W}}}$  is a diagonal weighting matrix. The weights are determined according to prescription by Huber (1964) (see also Constable (1988)) using the modulus of the data misfit

$$\mathbf{w} = \min \left( \frac{c}{|\mathbf{d} - \underline{\underline{\mathbf{G}}}\mathbf{m}|}, 1 \right) , \quad (4.25)$$

where  $c$  is chosen to be 1.5 times a prior estimate of the standard deviation of the data,  $\sigma_{prior}$ ,

$$c = 1.5 \cdot \sigma_{prior} \quad (4.26)$$

and the full weighting matrix involving both the Huber weights from equation 4.25 and the prior data error variances  $\sigma^2$  is then defined as

$$\mathbf{W} = \text{diag} \left( \frac{\mathbf{w}}{\sigma_{prior}^2} \right) . \quad (4.27)$$

We also choose to minimize the L2 norm of the model parameters, in an attempt to reduce the amount of superfluous structure in the resulting model. This is done by adding to the objective function a term

$$P(\mathbf{m}) = \mathbf{m}^T \underline{\underline{\mathbf{I}}}\mathbf{m} , \quad (4.28)$$

where  $\underline{\underline{\mathbf{I}}}$  is the identity matrix. With this addition, we arrive at an objective function  $J(\mathbf{m})$  given by

$$J(\mathbf{m}) = E(\mathbf{m}) + \alpha^2 P(\mathbf{m}) \quad (4.29)$$

$$J(\mathbf{m}) = (\mathbf{d} - \underline{\underline{\mathbf{G}}}\mathbf{m})^T \underline{\underline{\mathbf{W}}}(\mathbf{d} - \underline{\underline{\mathbf{G}}}\mathbf{m}) + \alpha^2 \mathbf{m}^T \underline{\underline{\mathbf{G}}}_1 \mathbf{m} . \quad (4.30)$$

The constant  $\alpha^2$  which the  $P(\mathbf{m})$  term is multiplied by is known as the regularization or damping parameter. It controls the trade-off between minimizing the data misfit and the norm of the model parameters, so that a higher value of  $\alpha^2$  serves to further reduce the norm of the monopole amplitudes and a lower value prioritizes fitting the data better. To minimize the objective function, the partial derivative of the function with respect to the model parameters is set equal to zero, leading to an expression for calculating the model parameters

$$\mathbf{m} = (\underline{\underline{\mathbf{G}}}^T \underline{\underline{\mathbf{W}}}\underline{\underline{\mathbf{G}}} + \alpha^2 \underline{\underline{\mathbf{G}}}_{inv}^T \underline{\underline{\mathbf{G}}}_{inv})^{-1} \underline{\underline{\mathbf{G}}}^T \underline{\underline{\mathbf{W}}}\mathbf{d} . \quad (4.31)$$

When the model parameters have been found, a resolution matrix  $\underline{\underline{\mathbf{R}}}_m$  may be calculated as

$$\underline{\underline{\mathbf{R}}}_m = (\underline{\underline{\mathbf{G}}}^T \underline{\underline{\mathbf{W}}}\underline{\underline{\mathbf{G}}} + \alpha^2 \underline{\underline{\mathbf{G}}}_{inv}^T \underline{\underline{\mathbf{G}}}_{inv})^{-1} \underline{\underline{\mathbf{G}}}^T \underline{\underline{\mathbf{W}}}\underline{\underline{\mathbf{G}}} , \quad (4.32)$$

along with a model covariance matrix

$$\underline{\underline{\mathbf{C}}}_m = \frac{E(\mathbf{m})}{N - \text{Tr}(R)} (\underline{\underline{\mathbf{G}}}^T \underline{\underline{\mathbf{W}}}\underline{\underline{\mathbf{G}}} + \alpha^2 \underline{\underline{\mathbf{G}}}_{inv}^T \underline{\underline{\mathbf{G}}}_{inv})^{-1} , \quad (4.33)$$

where  $N$  is the number of data points. This allows us to calculate the predictive covariances

$$\underline{\underline{\mathbf{C}}}_{pred} = \underline{\underline{\mathbf{G}}}\underline{\underline{\mathbf{C}}}_m \underline{\underline{\mathbf{G}}}^T . \quad (4.34)$$

The square root of the diagonal entries in this covariance matrix provides us with the predictive uncertainties.

#### 4.4.2 Estimation of prior data errors from covariances

A starting point is needed for the iterative least squares method, and in this case an inversion is performed that foregoes the Huber weights and instead uses only the inverse of an estimate of the data covariances  $\sigma_{prior}^2$  as weights. These covariance estimates are calculated differently for the satellite and for the observatory data, but they are both based on predictions made with the CHAOS-6 model (Finlay et al., 2016). For the satellites, the CHOAS predictions are subtracted from the measurements, and these residuals are then grouped into bins of size  $5^\circ$  according to their quasi-dipole latitude. A Huber weighted average of the residuals in each bin is calculated, and the standard deviation is then calculated as the root-mean-square misfit of the residuals with the Huber weighted average

$$\sigma_{prior} = \sqrt{\frac{\sum_{i=1}^N w_i (\epsilon_i^2 - \mu_{\epsilon,i}^2)}{\sum_{i=1}^N w_i}} . \quad (4.35)$$

Here  $w_i$  are the Huber weights,  $\epsilon_i$  are the residuals and  $\mu_\epsilon$  are the Huber weighted mean values of the residuals in a given bin. The standard deviations of data positions between bin centres are then given by spline interpolation, and a diagonal matrix of the inverse covariance is calculated

$$\underline{\underline{\mathbf{C}}}_{prior}^{-1} = \text{diag} \left( \frac{1}{\sigma_{prior}^2} \right) . \quad (4.36)$$

The initial model parameters can then be calculated by

$$\mathbf{m} = (\underline{\underline{\mathbf{G}}}^T \underline{\underline{\mathbf{C}}}_{prior}^{-1} \underline{\underline{\mathbf{G}}} + \alpha^2 \underline{\underline{\mathbf{G}}}_{inv}^T \underline{\underline{\mathbf{G}}}_{inv})^{-1} \underline{\underline{\mathbf{G}}}^T \underline{\underline{\mathbf{C}}}_{prior}^{-1} \mathbf{d} . \quad (4.37)$$

For observatory SV data, CHAOS predictions are once again subtracted from the measurements, and the residuals are de-trended. This is done by calculating the best straight-line fit to the residuals, which is then subtracted. The covariance of the de-trended residuals is then calculated, and the matrix is subsequently inverted.

### 4.4.3 L1 inversion for a sparse model

The solution described above is effective at reducing the amount of structure but also has some less desirable side-effects. Minimizing the L2 norm of monopole amplitudes tends to artificially suppress the amplitude and smooth the features of the model, which means that any piece-wise constant or "blocky" features are left unresolved. This is undesirable, as such structures may be of physical interest from an interpretative perspective. To remedy this, an L1 norm of  $B_r$  at the core surface can be used instead, as described by Farquharson and Oldenburg (1998). The conventional method of determining the L1 norm of some vector  $\mathbf{x}_j$ ,  $j = 1, \dots, I$  is given by

$$\|\mathbf{x}\|_1 = \sum_{j=1}^I |\mathbf{x}_j| , \quad (4.38)$$

but the use of moduli can in some instances cause computational difficulties, so a perturbed form is used instead

$$\underline{\underline{\mathbf{R}}} = \text{diag}((\mathbf{x}^2 + \epsilon^2)^{-1/2}) , \quad (4.39)$$

where  $\epsilon$  is a constant that needs to be small relative to the size of  $\mathbf{x}_j$ . We previously used the L2-norm regularization directly on the model parameters, now however, we regularize the L1 norm of  $B_r$  using a spherical grid of Lebedev quadrature points at the core surface

$$\underline{\underline{\mathbf{R}}} = \text{diag}((\mathbf{w}_l(\underline{\underline{\mathbf{G}}}_l \mathbf{m})^2 + \epsilon^2)^{-1/2}) , \quad (4.40)$$

where  $\mathbf{w}_l$  are the weights associated with the Lebedev quadrature points. From this expression we arrive to a new L1 definition for  $P(\mathbf{m})$

$$P_{L1}(\mathbf{m}) = \mathbf{m}^T \underline{\underline{\mathbf{G}}}_1^T \underline{\underline{\mathbf{R}}}_1 \underline{\underline{\mathbf{G}}}_1 \mathbf{m} . \quad (4.41)$$

As the expression for  $E(\mathbf{x})$  remains unchanged, the new objective function for the L1 solution is

$$\phi_{L1}(\mathbf{m}) = (\mathbf{d} - \underline{\underline{\mathbf{G}}}\mathbf{m})^T \underline{\underline{\mathbf{W}}}(\mathbf{d} - \underline{\underline{\mathbf{G}}}\mathbf{m}) + \alpha^2 \mathbf{m}^T \underline{\underline{\mathbf{G}}}_{\text{inv}}^T \underline{\underline{\mathbf{R}}}\underline{\underline{\mathbf{G}}}_{\text{inv}} \mathbf{m} , \quad (4.42)$$

and therefore the  $\mathbf{m}_{L1}$  that minimizes the above objective function is

$$\mathbf{m}_{L1} = (\underline{\underline{\mathbf{G}}}_{\text{inv}}^T \underline{\underline{\mathbf{W}}}\underline{\underline{\mathbf{G}}} + \alpha^2 \underline{\underline{\mathbf{G}}}_{\text{inv}}^T \underline{\underline{\mathbf{R}}}\underline{\underline{\mathbf{G}}}_{\text{inv}})^{-1} \underline{\underline{\mathbf{G}}}_{\text{inv}}^T \underline{\underline{\mathbf{W}}}\mathbf{d} \quad (4.43)$$

in this case, the L2 solution is used as a starting set of model parameters for the iteration.

## 4.5 Choice of the modelling hyperparameters

There are some free modelling hyperparameters that have an important impact on the inversion results, and appropriate values of these parameters need to be determined. Two important hyperparameters are the radius of the monopole grid, and the amount of monopoles it contains. In theory, increasing the number of monopoles should allow a closer fit to the data, but it also makes the computations more cumbersome, so this is more a matter of practicality: We need to find a grid configuration that provides an acceptable fit while still being within reasonable computational limits.

Other hyperparameters relate to the time-dependence. These are both the choice of covariance function, and also the value of the characteristic time scale  $\tau$ . This should be chosen to best fit the data, so an investigation of how well different models fit the observatory measurements will be performed. The final parameter that needs to be chosen is the regularization parameter  $\alpha^2$ , which controls the trade-off between fitting the data closely and minimizing the level of detail in the model.

### 4.5.1 Configuration of the monopole grid

As the resulting models obtained by the inversion are dependent upon the configuration of the monopole grid, a series of tests was carried out in order to determine an appropriate configuration of the grid. Two parameters define the spherical monopole grid: The depth within the core, specified by the radius of the spherical grid, and the amount of monopoles on the spherical surface.

Ideally, the grid should be placed as near to the core surface and with as many monopoles as possible, as this will allow us to accurately fit the data, as well as decrease the L1 norm of  $B_r$  at the core surface as much as possible, in order to show the interesting, sparse structures in the resulting model. If a too small grid radius is used, the resulting models will be smoothed and the L1 behaviour will be suppressed; similarly it will not possible to accurately fit the data if too few monopoles are used.

There are however limits to how large the grid radius can get, as the monopoles will eventually come so close to the core surface that individual monopoles will be visible in the resulting model, which is clearly un-physical. Likewise, there is a limit to how many monopoles that can be placed in the grid, as once a certain number of monopoles is reached, they will come so close to each other that the rows of the design matrix  $\underline{\underline{\mathbf{G}}}$  will become

Monopoles	400	600	800	1000
Iterations	119	200	200	200
L1-change [%]	0.099	0.104	0.150	0.278
MAD-misfit [nT]	6.0923	6.3729	6.5823	6.5635
Cond(G)	$1.3637 \cdot 10^9$	$1.8012 \cdot 10^{11}$	$1.2697 \cdot 10^{13}$	$3.987 \cdot 10^{14}$
L1-norm [mT]	3.0049	3.0049	2.8712	2.8551

Table 4.2: Grid radius: 0.7323c.

Monopoles	400	600	800
Iterations	113	197	200
L1-change [%]	0.099	0.099	0.51
MAD-misfit [nT]	6.1328	6.3427	7.1695
Cond(G)	$5.1768e \cdot 10^9$	$9.3128 \cdot 10^{11}$	$8.3562 \cdot 10^{13}$
L1-norm [mT]	3.0053	2.91854	2.8486

Table 4.3: Grid radius: 0.6866c.

linearly dependent, resulting in rank-deficiency, and hence a large condition number, which creates computational problems. Increasing the amount of monopoles also greatly increases the time it takes to compute a time-dependent model, so a compromise will have to be made. To help in choosing the grid radius and total amount of monopoles, a number of different test runs have been carried out, all with the following inversion method:

- No time dependence, the model is static.
- L1 norm regularization of  $B_r$  at the core surface, using a Lebedev grid consisting of 2702 points. Regularization parameter is picked by the knee of the L-curve method.
- Iteratively re-weighted least squares method, using Huber weights.
- Monopole grid made by recursive zonal equal area sphere partitioning.
- Every 100th data point from a dark data set is used, which consists of measurements from the Swarm A satellite made from February 14 to February 15.
- Iteration continues until the change in the L1-norm of the model parameters is less than  $10^{-4}$ , or until the 200th iteration.

A number of different parameters characterizing each model is noted:

- The number of iterations needed to reach convergence.
- The L1 norm change of the model parameters in the final iteration.
- The MAD-misfit of predicted values of the magnetic field with respect to the data.
- The condition number of the  $\underline{\underline{\mathbf{G}}}$  matrix.
- The L1 norm of  $B_r$  at the core surface.

Monopoles	400	600	Monopoles	200	400
Iterations	200	200	Iterations	43	200
L1-change [%]	0.154	0.359	L1-change [%]	0.099	0.441
MAD-misfit [nT]	6.1269	8.0553	MAD-misfit [nT]	6.2205	6.7946
Cond(G)	$2.1487e \cdot 10^{10}$	$5.3796 \cdot 10^{12}$	Cond(G)	$9.585 \cdot 10^7$	$9.8779 \cdot 10^{10}$
L1-norm [mT]	3.0041	2.8349	L1-norm [mT]	3.1933	2.9262

Table 4.4: Grid radius: 0.6408c

Table 4.5: Grid radius: 0.5950c

An appropriate configuration of the monopole grid will involve a small MAD-misfit, be sufficiently converged with respect to the change in the L1 norm of the model parameters and have as small an L1-norm of  $B_r$  at the core surface as possible, but with sufficiently few monopoles as to not be too computationally cumbersome when inverting for a time-dependent model using a large dataset. Models are calculated at four different radii: 0.7323c, 0.6866c, 0.6408c and 0.5950c, with  $c$  being the core radius, here set to 3480.0 km. Five different numbers of monopoles are used: 200, 400, 600, 800 and 1000. Note however that not all of these amounts of monopoles are feasible at every given radius, since 200 is too few to fit the data at large radii, and 1000 is too many for the rows of the  $\underline{\underline{\mathbf{G}}}$  matrix to be linearly independent at smaller radii. Figures 4.2 and 4.3 summarize the results: the MAD-misfit as a function of the grid radius, and the L1 norm of  $B_r$  at the core surface as a function of the amount of monopoles, along with the associated condition numbers of the  $\underline{\underline{\mathbf{G}}}$  matrix.

When looking at figure 4.2, it can be seen that for a fixed number of monopoles, the misfit increases as the radius becomes too small, but the misfit is lower for fewer monopoles,

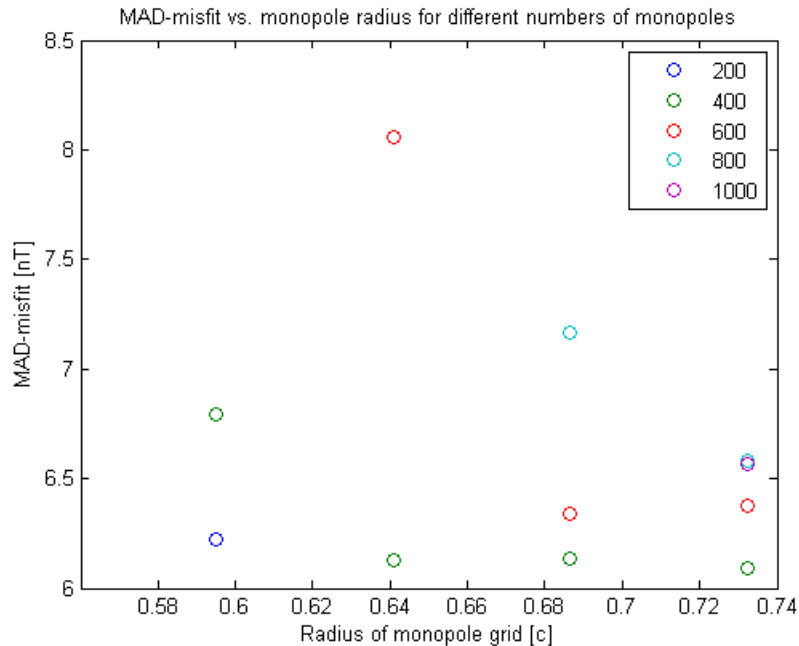


Figure 4.2: The MAD misfits of the calculated models plotted against the monopole grid radius. The colours indicate the number of monopoles.

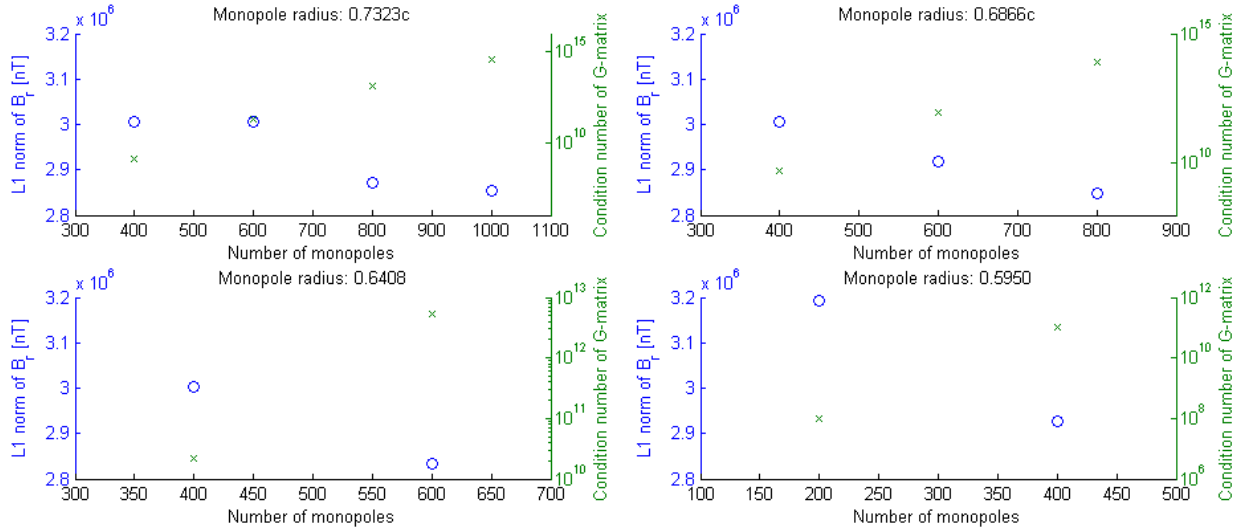


Figure 4.3: Plots of the norm of  $B_r$  for different numbers of monopoles, at the four chosen grid radii.

which is contrary to what would be expected, but this is most likely since a higher amount of monopoles more effectively decreases the L1 norm of  $B_r$ , at the expense of fitting the data slightly worse. All of the misfits are however very similar, except for 600 monopoles at 0.64c, which is due to the aforementioned problem with rank-deficiency. It is obvious from figure 4.3 that the maximum number of monopoles at a given radius gives the lowest possible  $B_r$  norm, they all seem to converge to a about  $2.85 \cdot 10^6$  nT. Choosing a grid that results in this low value of the norm is however not practically feasible, as can be seen from the associated condition numbers of the design matrix  $\mathbf{G}$ . The rank-deficiency problems results in these models not being fully converged with respect to the relative change in model parameters and therefore ill-behaved, as can be seen from the shape of the associated L-curves, see figure 4.4. The case of 600 monopoles is fairly L-shaped, with sensible values of misfit and model norm, and a clearly defined corner. This becomes gradually worse as the amount of monopoles is increased, ending with a mess for 1000 monopoles.

These tests reveal that a monopole grid consisting of 600 monopoles at a radius of 0.6866c should be the most appropriate. This grid gives a low misfit of 6.343 nT, an L1 norm of  $B_r$  at the core surface of  $2.9185 \cdot 10^6$  nT, which is only 2.2% larger than the value achieved with 1000 monopoles at 0.7323c. The model resulting from this grid sufficiently converged, as to have a change in L1 norm of the model parameters of less than 1% after 197 iterations. However, when carrying out a time-dependent inversion, a compromise has to be made between the number of monopoles and the number of reference times the monopole amplitudes are defined at, in order for the  $\underline{\underline{\mathbf{G}}}$  matrix to not be too large. We don't want the separation between reference times to be larger than 1 year, which means that 500 is the limiting amount of monopoles. The grid chosen as the most appropriate for the time-dependent inversion is therefore of radius 0.6866c, with 500 monopoles.

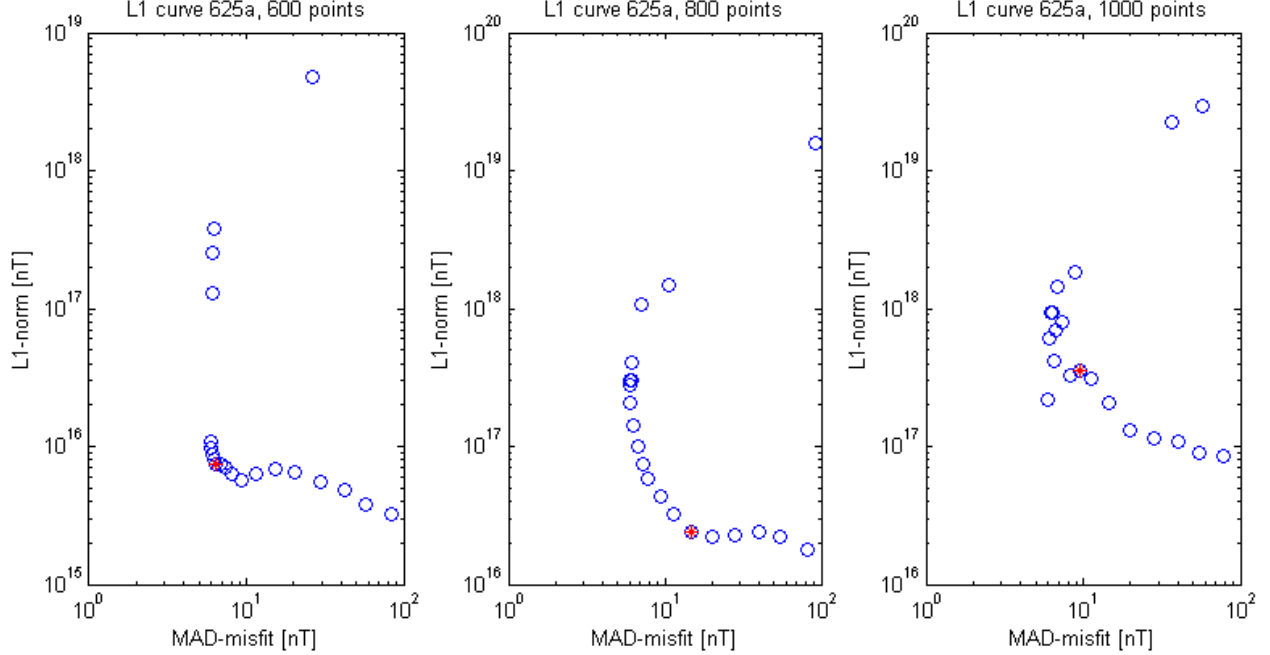


Figure 4.4: Three different L-curves for 600, 800 and 1000 monopoles, at 0.6866c, showing the increasingly bad behaviour due to rank deficiency of the G-matrix.

#### 4.5.2 Covariance function and characteristic time scale $\tau$

To determine the optimal value of the characteristic time scale  $\tau$ , and to test which covariance function is most appropriate for modelling the observed secular variation, a series of tests were performed where these parameters are varied. The tests all have the following characteristics:

- L2 regularization of the monopole amplitudes.
- The entire data set is used, consisting of three components of the secular variation from the observatories, and r-component main field measurements from CHAMP and Swarm.
- Number of monopoles set to  $M = 200$  for faster computation, monopole grid radius is set to 0.686c.
- Reference times of the monopoles are 22 linearly spaced points between the years 1997.1 and 2016.7.
- Value of  $\alpha^2$  determined to be  $6 \cdot 10^{-23}$  through the knee of the L-curve method.

Tests are performed for both the squared exponential, and Matérn ( $\nu = 3$ ) covariance functions. Values of  $\tau$  tested are 1000, 3000, 5000 and 7000 days. The root mean square of the residual of the predicted data with the observed is noted down, along with the L2-norm of the model parameters and the total weighted misfit calculated as

$$\text{misfit} = \sqrt{\frac{E(\mathbf{m})}{N}} \quad (4.44)$$

$\tau$	Matern		SE	
	L2-norm [ $10^{13}$ nT]	Weighted misfit	L2-norm [ $10^{13}$ nT]	Weighted misfit
1000	1.4319	2.0578	3.7218	1.1763
3000	1.0713	1.1844	3.2966	1.2140
5000	1.0927	1.0739	2.7121	1.2780
7000	1.1725	1.0473	4.5659	1.3484

Table 4.6: The L2 model norms as well as weighted misfits for the different models considered in this test.

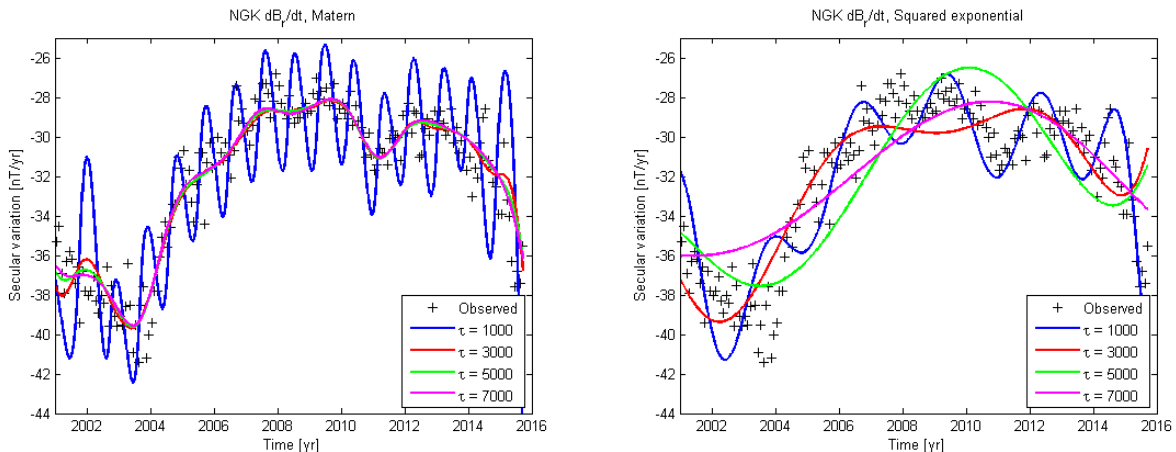


Figure 4.5: Left: Model predictions of the SV at Niemegk for the four different values of  $\tau$  using a Matern ( $\nu = 3$ ) covariance function. Right: The same, but with a squared exponential covariance function.

$N$  being the number of data. This should have a value close to unity if the fit is good, see table 4.6. Beyond this, the model predictions are compared to the observed secular variation at the Niemegk observatory in Germany, see figure 4.5. It is clear from the comparison to Niemegk that the squared exponential function has a hard time fitting the fast changes observed here.  $\tau = 1000$  days is a bit too short, and  $\tau = 3000$  days is already too long, although the fit in between might be better, sharp changes still won't be captured. When looking at the Matern covariance function,  $\tau = 1000$  days is also too short a characteristic time scale, but after this the models seem to converge. The Matern function, with its ability to fit "rough" time dependence, is clearly not as sensitive to the choice of  $\tau$  as the SE. When looking at figure 4.6, it can be seen that the case of  $\tau = 7000$  days has a slightly better fit to the r-component of the observatory data set when compared to  $\tau = 5000$  days, but also has a higher model norm. An appropriate characteristic time scale of  $\tau = 6000$  days is therefore chosen as a compromise between these two.

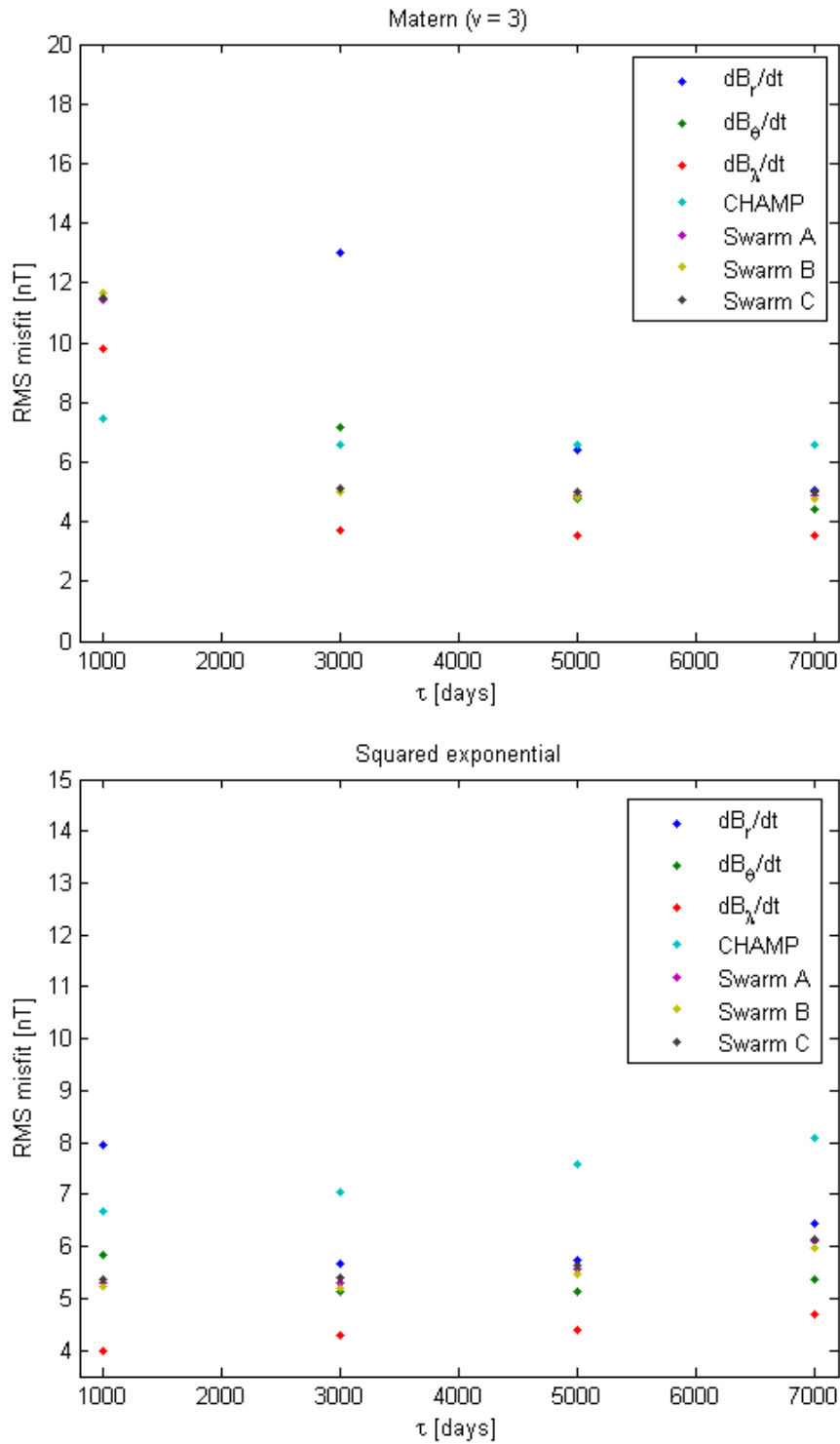


Figure 4.6: Top: The RMS misfit of each data set as a function of  $\tau$  for the Matern covariance function. Bottom: The same for the SE covariance function.

### 4.5.3 Regularization parameter $\alpha^2$

A simple if time-consuming way of determining the regularization parameter is by calculating an ensemble of models that only differ in the choice of  $\alpha^2$ , and then plotting the (L1 or L2) norm as a function of the misfit norm in a double-logarithmic plot. This should result in a more or less L-shaped curve, and the optimal value of  $\alpha^2$  is then the point of maximum curvature, which is also why this method is usually called finding the "knee" of the L-curve, see figure 4.4 for an example.

# Chapter 5

## Results

In this section, the results of the two different inversions that have been carried out will be presented, along with figures that characterise both the quality of the fit to the data, but also the predictive power of the model.

### 5.1 A time-dependent L2-regularized monopole-based field model

Here we present first results from a model that regularizes the L2 norm of the monopole amplitudes, constructed by computing

$$\mathbf{m} = (\underline{\underline{\mathbf{G}}}^T \underline{\underline{\mathbf{W}}}\underline{\underline{\mathbf{G}}} + \alpha^2 \underline{\underline{\mathbf{I}}})^{-1} \underline{\underline{\mathbf{G}}}^T \underline{\underline{\mathbf{W}}}\mathbf{d} \quad (5.1)$$

with the previously discussed favoured monopole grid parameters ( $r = 0.686c$ ,  $M = 500$ ), and with the time-dependence given by a Matérn ( $\nu = 3$ ) covariance function with a characteristic

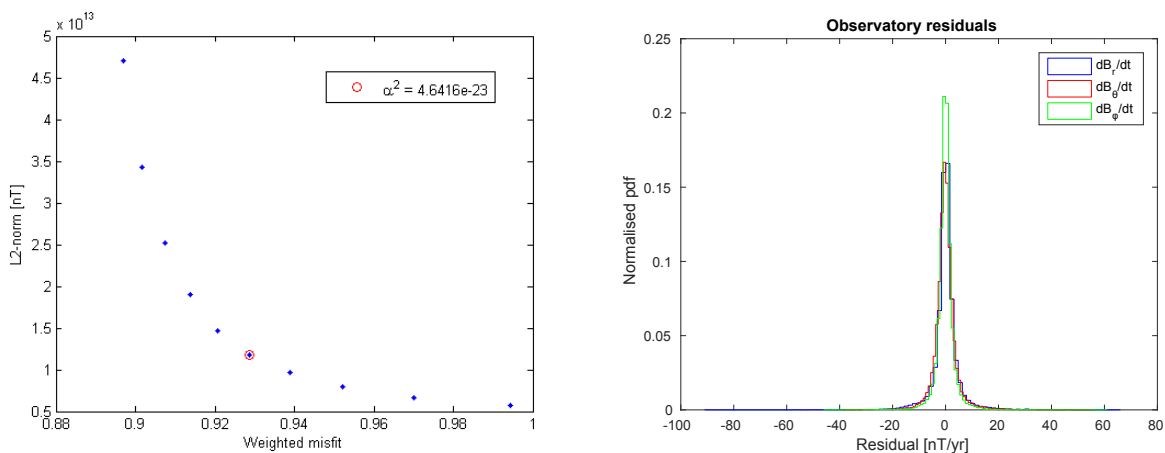


Figure 5.1: Left: L-curve for 10 different models with values of  $\alpha^2$  spanning from  $10^{-24}$  to  $10^{-21}$ , the knee is indicated by the red circle. Right: Histogram of residuals from the observatory data, blue being radial component, red is lateral and green is longitudinal.

Data set:	Obs <sub>r</sub>	Obs <sub>θ</sub>	Obs <sub>φ</sub>	CHAMP	Swarm A	Swarm B	Swarm C
Weighted RMS misfit:	1.0036	0.9889	0.8627	0.9084	0.9068	0.9170	0.9037

Table 5.1: Weighted root-mean-square misfits to the individual data sets used in the inversion.

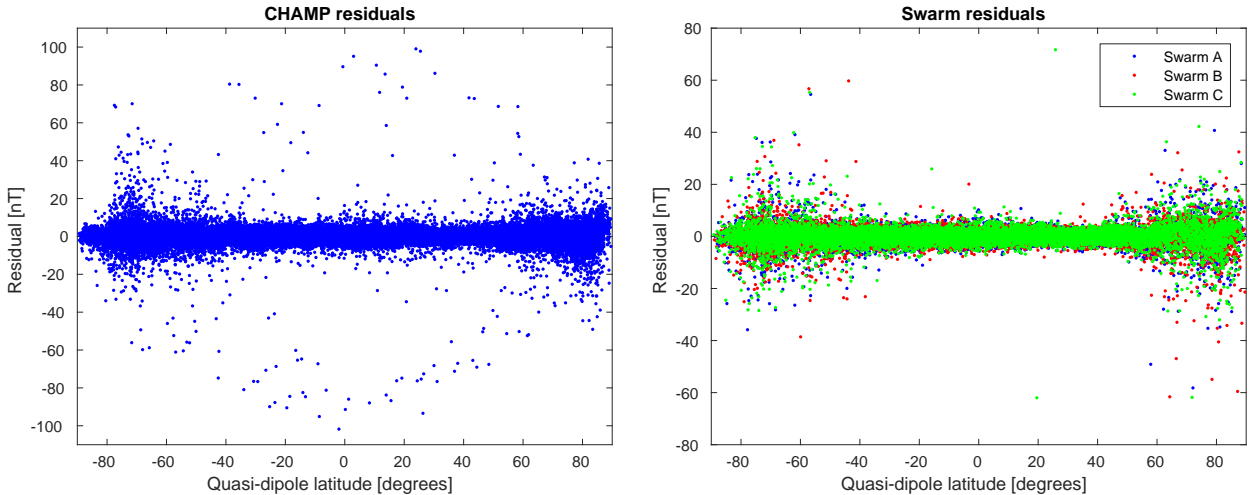


Figure 5.2: Residuals of the satellite measurements as a function of quasi-dipole latitude. Left: CHAMP. Right: Swarm A (blue), B (red) and C (green).

time scale of  $\tau = 6000$  days, and with the reference times of the monopoles at 22 linearly spaced points between the years 1997.1 and 2016.7. The value of  $\alpha^2$  has been determined by an L-curve (see figure 5.1 left) to be  $\alpha^2 = 4.641610^{-23}$ . This results in a total weighted misfit of 0.9288 and the L2 norm of the model parameters is  $1.18 \cdot 10^{13}$  nT. The weighted RMS misfit of the predictions to each of the individual data sets can be seen in table 5.1.

The model clearly fits the data quite well, which can also be seen from the histograms of the residuals for the three different observatory components (figure 5.1 right) and from the plots of the satellite residuals as a function of geomagnetic quasi-dipole latitude, see figure 5.2. Besides a few large mid-latitude outliers, most of the larger residuals are in the auroral zones, which are more susceptible to contamination from the external fields, via the auroral electrojet (which is an internal source to satellites). The fit of the model to a few selected ground observatories can be seen in figure 5.3. The model clearly captures most of the secular variation, even though there are some fast, high amplitude changes for example in the  $\theta$ -component at Kakiopa, Japan, which are not completely captured by the model.

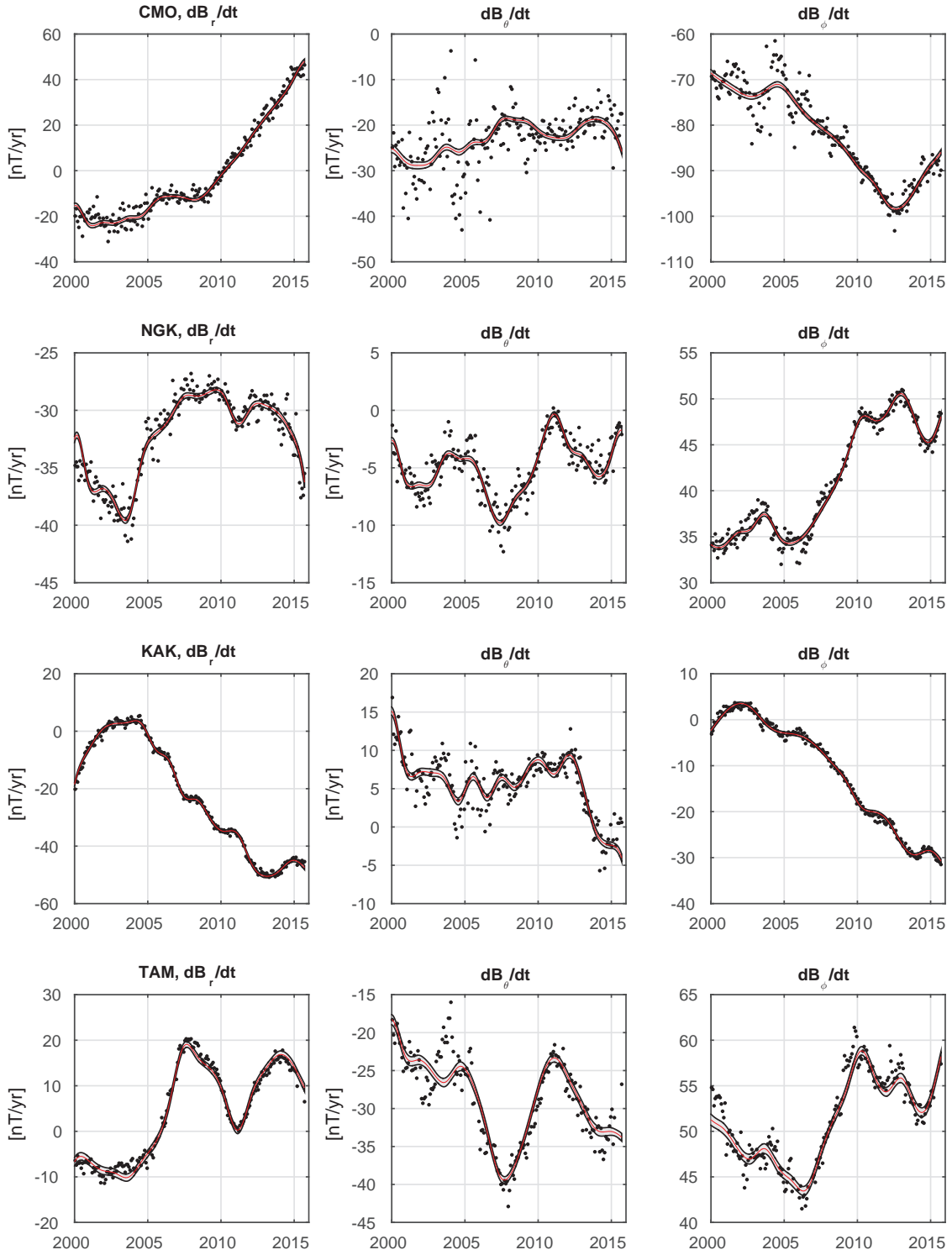


Figure 5.3: Fits to the four observatories at College in the USA (top), Niemegek in Germany (second from top), Kakiopa in Japan (third from top) and Tamanrasset in Algeria (bottom), for all three components,  $r$  (left)  $\theta$  (middle) and  $\phi$  (right). Black dots are annual differences of revised monthly means, red lines are SV predictions, and the gray envelope is  $\pm 2\sigma$ .

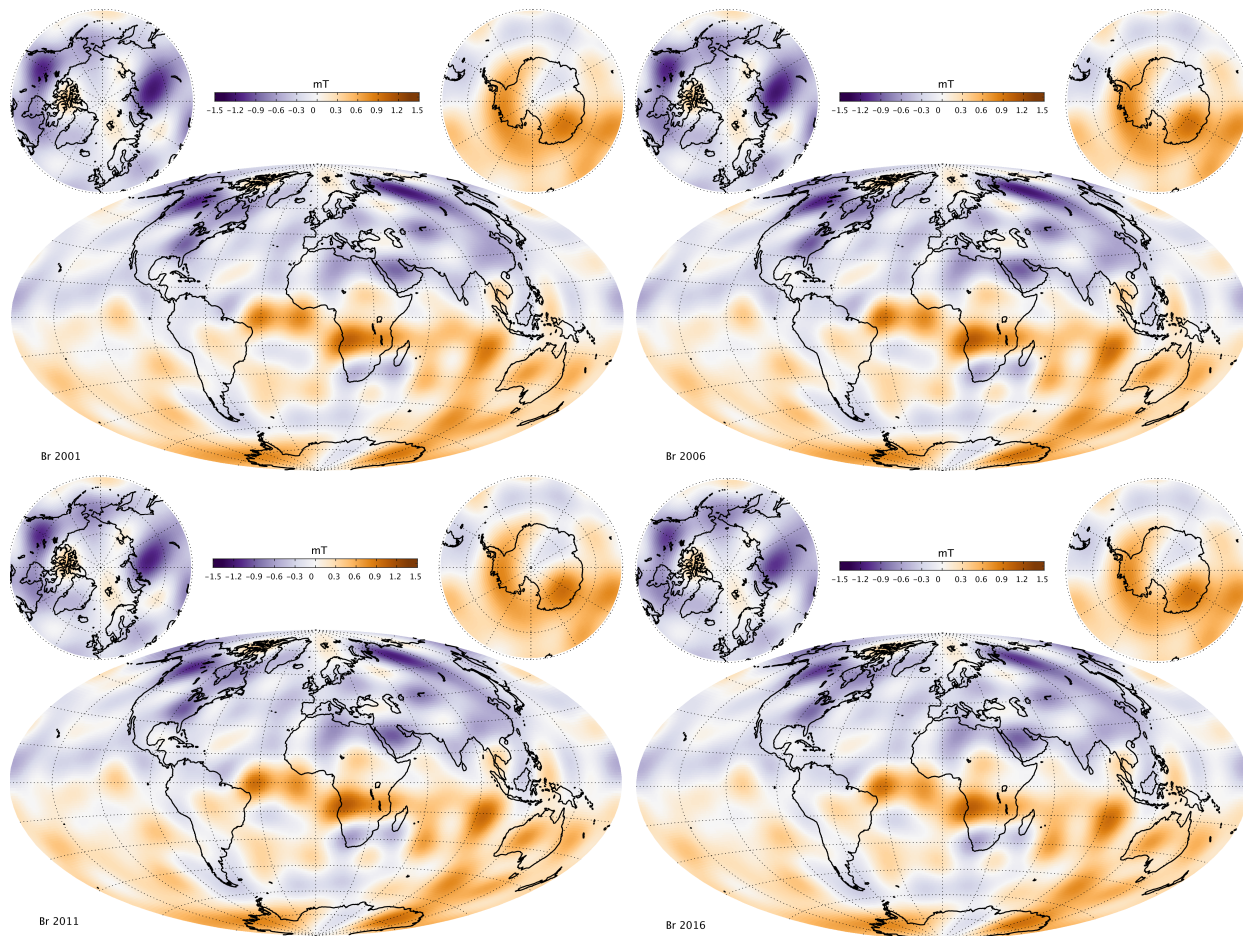


Figure 5.4: Model prediction of the radial B field at the core-mantle boundary, for 2001 (top left), 2006 (top right), 2011 (bottom left) and 2016 (bottom right). Projection is Hammer-Aitoff.

The radial component of the main field at the core-mantle boundary, approximately 3480 km below the Earth’s surface, is shown in figure 5.4. The short time span makes it difficult to discern at first glance, but one can identify the westward drift of the field features if one closely observes the patches of high radial field strength near the equator. This is also implied by figure 5.5, which shows the secular variation for the same times. Note that these are annual differences, so the SV at 2001 is given by main field at 2001 with the main field at 2000 subtracted from it, and so on. Most of the intense SV is in the area of the high intensity reverse flux patches at the equator, but there are also three intense patches in the northern hemisphere, around the Bering strait, which seem to increase in intensity during the model time span.

An estimate of the model uncertainties can be seen in figure 5.6, which shows the model standard deviation of the radial field component at the core mantle boundary, calculated by equations (4.32), (4.33) and (4.34). The standard deviation being the square root of the diagonal elements in the predictive covariance matrix. It can be seen that there are tiny spots of higher standard deviation centred on all of the monopoles, which are marked as

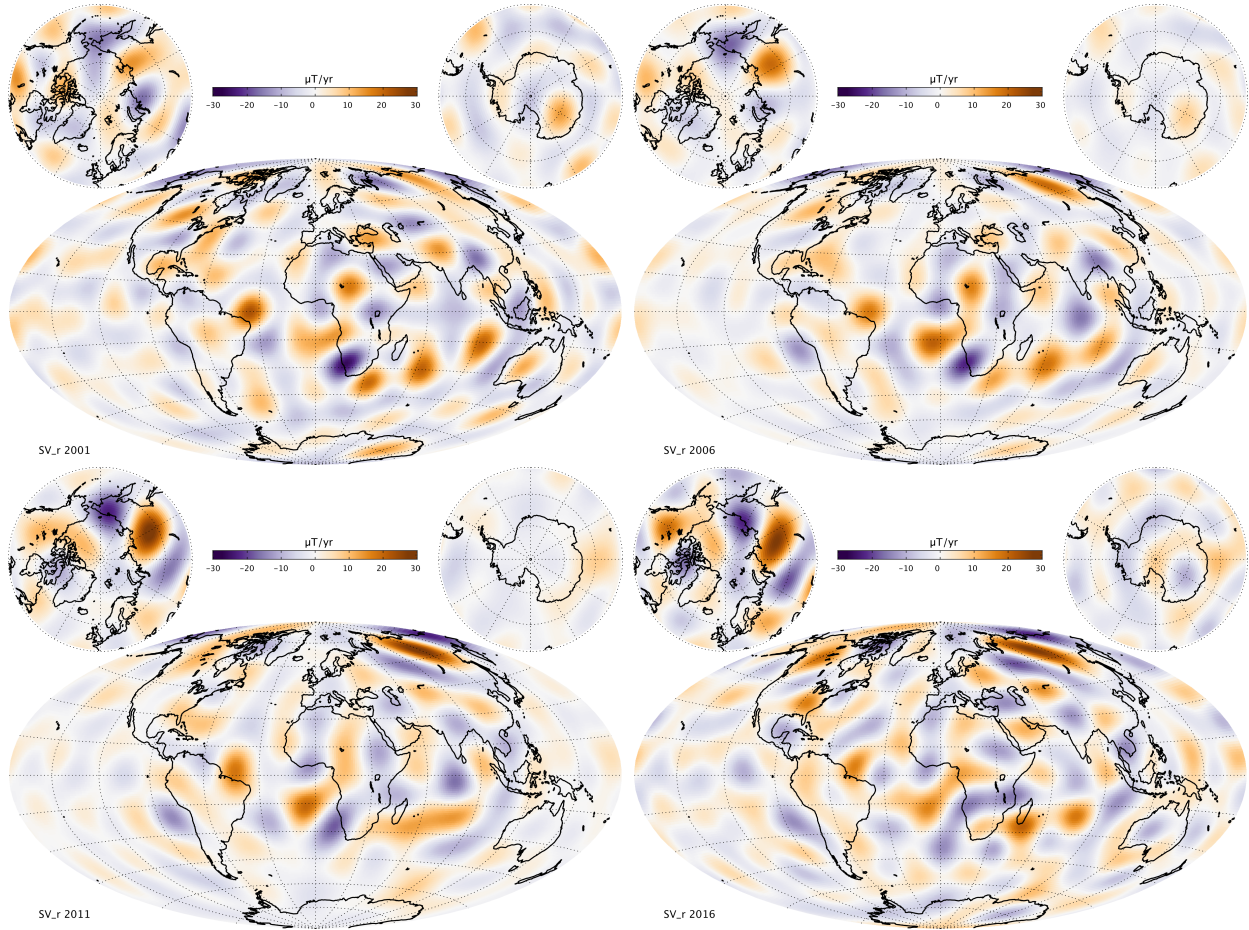


Figure 5.5: Model prediction of the radial secular variation at the core-mantle boundary, for 2001 (top left), 2006 (top right), 2011 (bottom left) and 2016 (bottom right). Projection is Hammer-Aitoff.

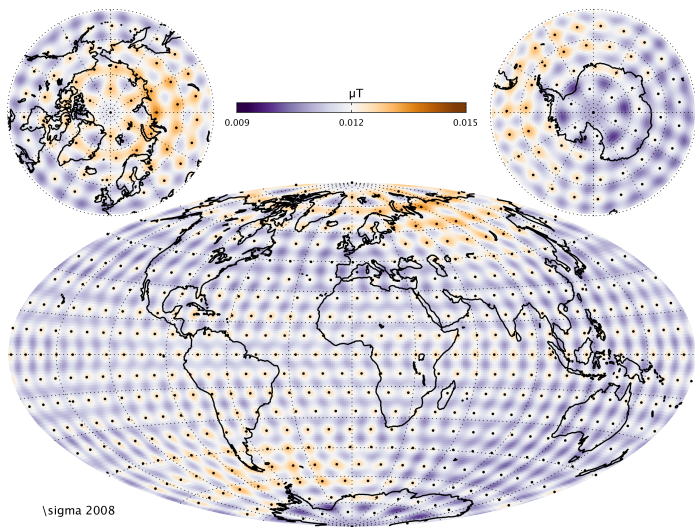


Figure 5.6: Plot of the standard deviation of the radial field component at the core mantle boundary. The Black dots are the positions of the monopoles. Projection is Hammer-Aitoff.

black dots. Beyond that, the standard deviation is highest in the northern polar area, and off the southern tip of America. The model standard deviation also seems to be slightly higher around the equator. Note however that the highest values of the standard deviation are approximately  $0.015 \mu\text{T}$ , which is around a  $1/1000$ th of a percent of the highest values of the radial field strength,  $1.5 \text{ mT}$ , so these standard deviations are very low.

## 5.2 L1-regularized monopole-based field model

Unfortunately, it was not possible to carry out a successful inversion for a time-dependent L1-regularized model, as the iteration never achieved convergence, see figure 5.7 (left). The reason for this failure is not quite apparent, but is definitely associated with the design matrix  $\underline{\underline{\mathbf{G}}}_{leb}$  which maps the monopole amplitudes to the radial field at the Lebedev points on the core surface. An inversion was performed without this design matrix, which would cause a minimization of the L1-norm of the monopole amplitudes, and a histogram of the resulting model parameters show a very clear Laplace distribution, see figure 5.7 (right). This suggests that the L1 norm measure of Farquharson and Oldenburg (1998) works as intended.

The problem might be connected to the fact that the  $\underline{\underline{\mathbf{G}}}_{leb}$  design matrix only serves to reduce the L1-norm of  $B_r$  at particular points in time, but changing the number of reference times did not seem to solve the problem, nor did increasing the amount of times the L1 norm was minimized, while keeping the same reference times. The condition number of the  $\underline{\underline{\mathbf{G}}}_{leb}$  is also quite high,  $4.3920 \cdot 10^9$ , which may serve to further exacerbate the difficulties in reaching convergence, as problems with ill-conditioning persisted even with very large values of  $\alpha^2$ . It was however possible to produce static L1 models, as can be seen from figure 5.8, which was made during the test of the monopole grid parameters.

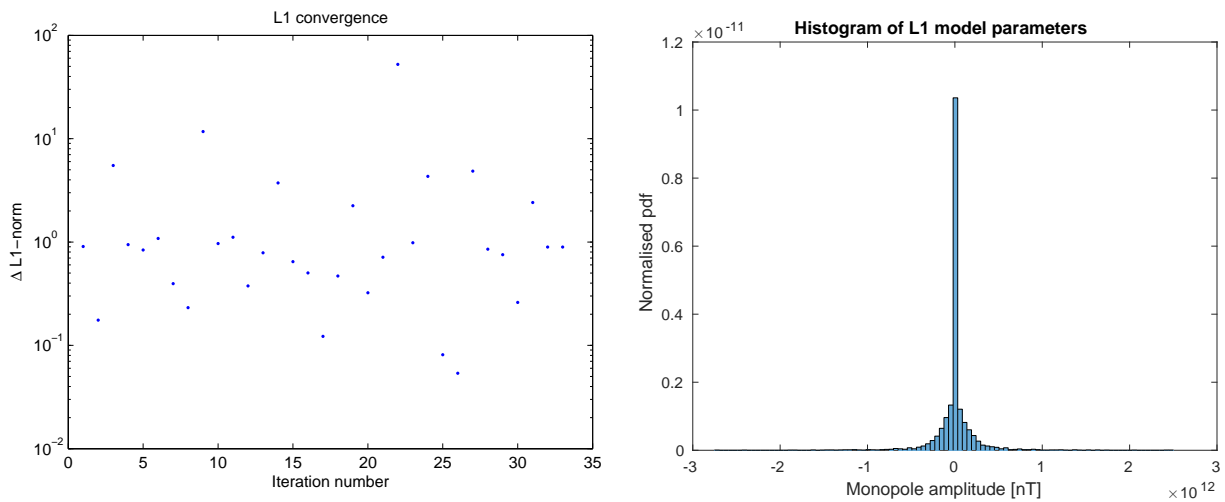


Figure 5.7: Left: Plot of relative change in the L1 norm of the model parameters as a function of iteration number. Right: Histogram of the model parameters when minimizing the L1 norm of monopole amplitudes.

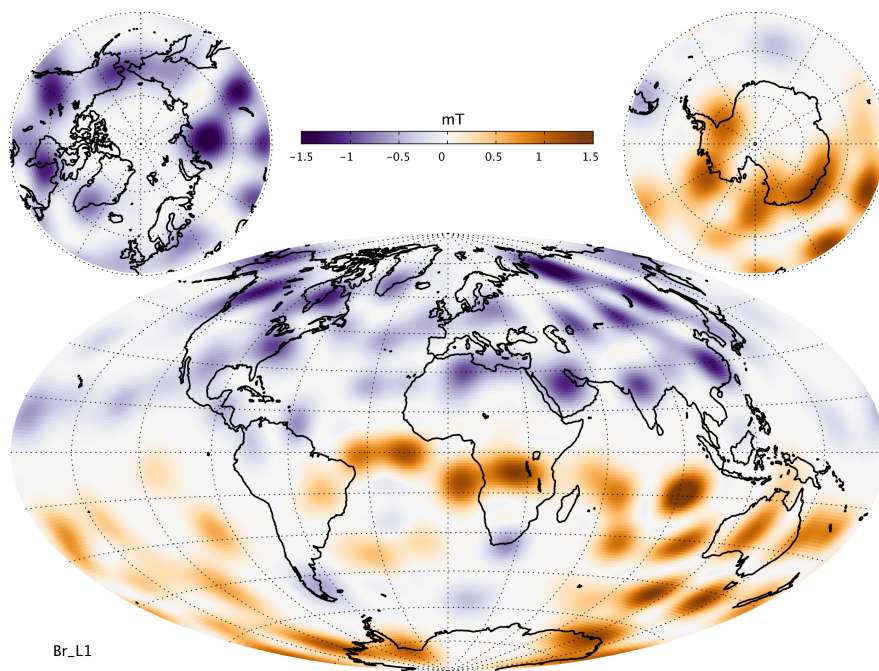


Figure 5.8: Map of the radial magnetic field at the core surface as predicted by a static L1 model using 600 monopoles and data from the Swarm A satellite. Hammer-Aitoff projection.

# Chapter 6

## Discussion

In this section, the predictive power of the L2-regularized monopole model will be compared to the CHAOS-5 and CHAOS-6 models. The fits to individual observatory time series will be compared, but also maps of the secular variation at the core surface. Additionally, the secular acceleration has also been calculated to see if the monopole model can reproduce the findings in Finlay et al. (2015). An investigation of the change in the unsigned flux of the monopole model has been carried out and is also presented here.

### 6.1 Comparison with CHAOS models

To help in characterising the robustness of the findings detailed in the results section, a comparison will be made between the predictions of the L2 regularized monopole model and those of the CHAOS-5 and CHAOS-6 models. The first comparison will be between fits to observatory time series, a few examples can be seen in figure 6.1. The monopole model seems to capture some features better than CHAOS-6, as can be seen by the time series at Honolulu from 2011 and onwards, but also from the two small bumps around 2002 and 2004. Neither of the two models are able to accurately reproduce the rapid changes in the first half of the time series at Kakioka, but the monopole model might do a slightly better job, particularly from 2011 and onwards. The same can be seen from the time series at Boulder, neither model seems to really capture the sharp peak at 2006, but the monopole model has a slightly better fit at the last half of the time series.

Overall however, the two models are very similar, and the differences are negligible in many of the time series, as can be seen from the comparison at Hermanus, as well when comparing the residuals from all observatories, see figure 6.2. The similarities are also quite apparent when comparing on a global scale, as can be seen from figure 6.3. The same mid-latitude features are visible in both models, though the intensities seem slightly higher in the CHAOS-6 model. The high intensity negative-positive-negative triplet in the northern polar region look almost exactly the same, and are increasing in strength in both models.

A comparison can also be made on model predictions of the secular acceleration (SA), which is the second time derivative of the main field. In Finlay et al. (2015), three distinct pulses of SA were identified at the core surface in 2006, 2009 and 2013. These pulses are thought to be the cause of the geomagnetic jerks that are visible in observatory time series,

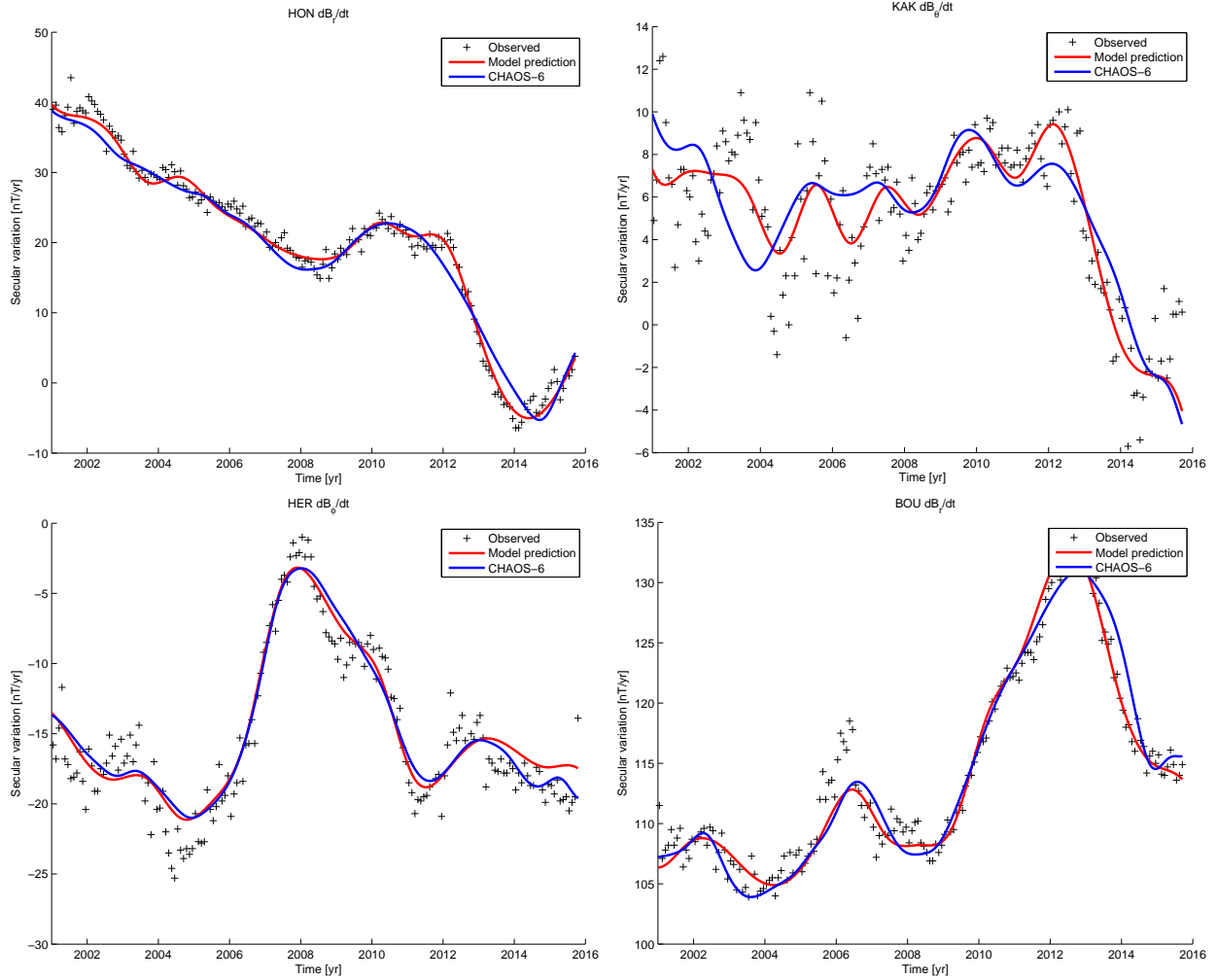


Figure 6.1: Comparison of predictions for the SV from L2 regularized monopole model and CHAOS-6 at 4 different observatories. Top left: The radial component at Honolulu, Hawaii. Top right: The  $\theta$  component at Kakioka, Japan. Bottom left: The  $\phi$  component at Hermanus, South Africa. Bottom right: The radial component at Boulder, Colorado.

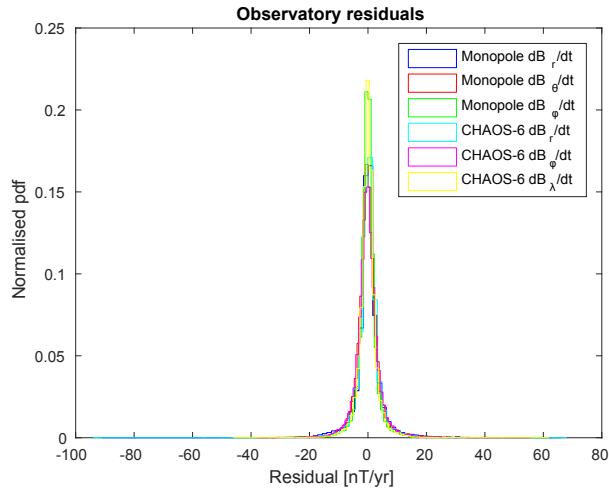


Figure 6.2: Comparison of residuals for the three different observatory data sets.

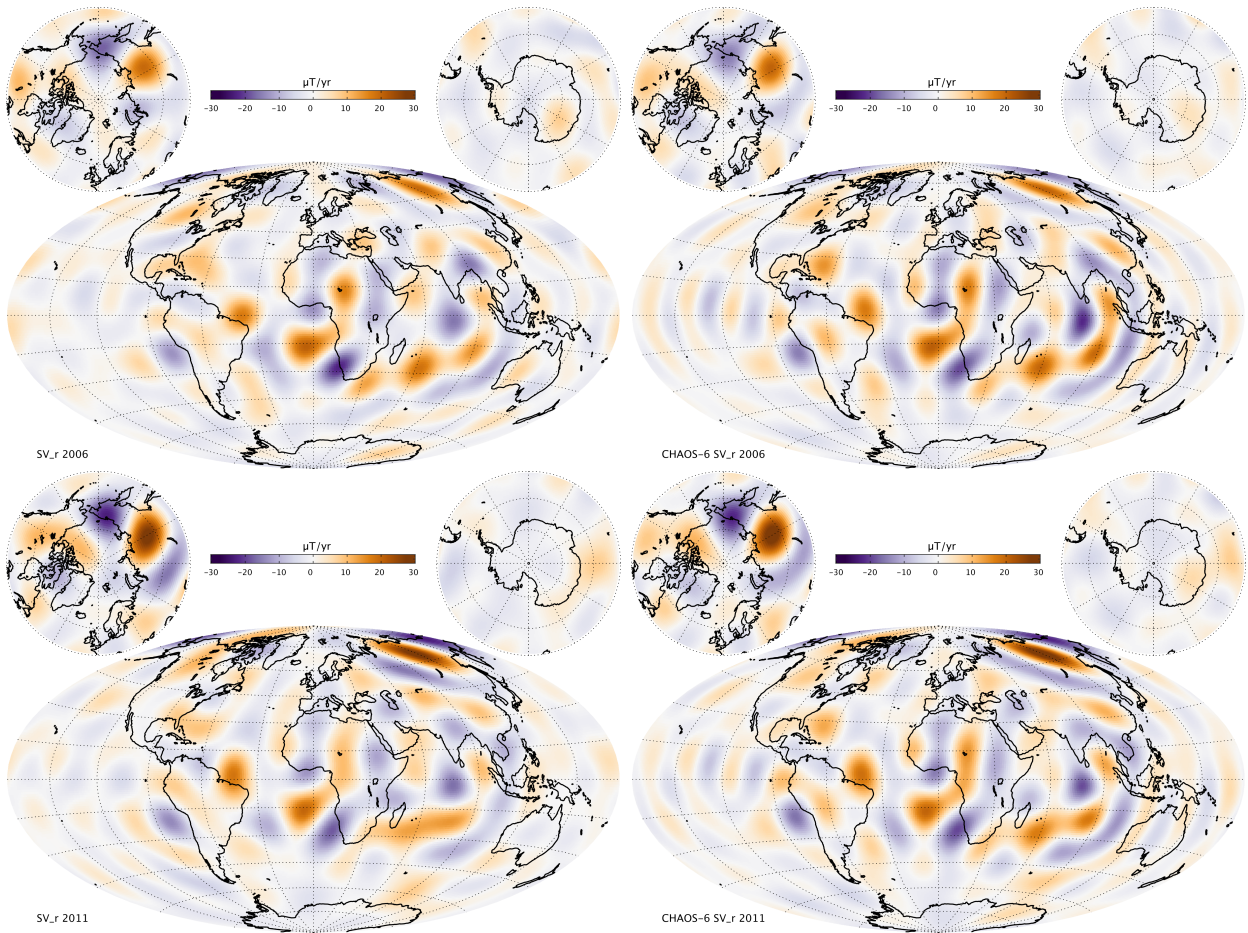


Figure 6.3: Comparison of predictions for the SV at the core-mantle boundary. Top left: Monopole model, 2006. Top right: CHAOS-6, 2006. Bottom left: Monopole model, 2011. Bottom right: CHAOS-6, 2011. Hammer-Aitoff projection.

and are therefore interesting to study. Large SA intensities were identified off the eastern coast of Brazil, see figure 6.4. This peak of intensity seems to be negative in 2006, positive in 2009 and negative again in 2013. Suggested explanations for this behaviour are oscillations in the geostrophic flow in the core, or fast magnetohydrodynamic waves in the outer layers of the core. To see whether the monopole model also resolves these SA pulses, an SA design matrix  $\underline{\mathbf{G}}_{SA}$  is calculated as the difference of two SV design matrices, in much the same way

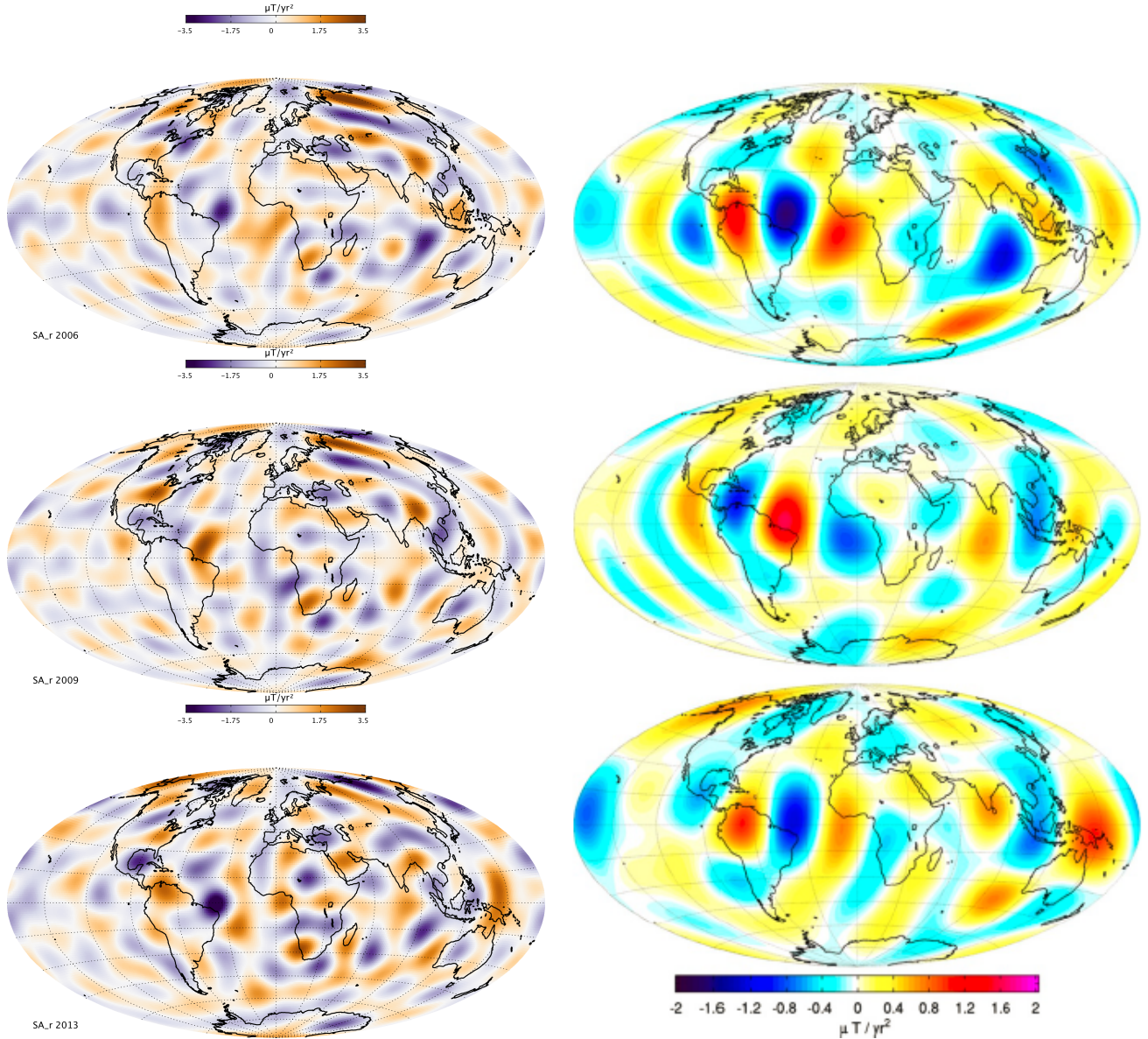


Figure 6.4: Left: SA at the core surface from the Monopole model at times 2006 (top), 2009 (middle) and 2013 (bottom). Right: SA at the core surface for the first 8 spherical harmonic degrees of the CHAOS-5 model, in 2006 (top), 2009 (middle) and 2013 (bottom). Hammer-Aitoff projection. From Finlay et al. (2015)

as the SV matrix was calculated as the difference between main field design matrices

$$\underline{\underline{\mathbf{G}}}^{SA} = \underline{\underline{\mathbf{G}}}^{SV}_j - \underline{\underline{\mathbf{G}}}^{SV}_i \quad (6.1)$$

with  $i$  being some time and  $j$  being  $j = i + 1$  yr. The maps of CHAOS-5 are truncated after spherical harmonic degree 8, so they have much less short-scale spatial structure than the ones made with the monopole model. The high intensity SA pulse off the eastern coast of Brazil is however clearly visible in the monopole model, going from negative in 2006 to positive and slightly smeared in 2009 and back to negative and very localized in 2013.

## 6.2 Changes in the unsigned flux

Since the validity of the frozen flux approximation has been called into question, and a debate is now ongoing, it could be interesting to investigate the change in the unsigned flux of the monopole model during the model time span, even though no attempt at constraining it has been made. The unsigned flux  $N$  is defined as

$$N = \int_S |\mathbf{B}_r| d\Omega, \quad (6.2)$$

$S$  being a spherical surface with radius  $c = 3480$  km. This integral is evaluated using Lebedev quadrature, and a time series of the unsigned flux is calculated, see figure 6.5. The percentage change in the unsigned flux over the 16 year model time span is calculated to be 1.4%, which is relatively small, but not negligible when considering the long time scales associated with secular variation.

The peculiar parabolic shape of the time series is however most likely not physical, but rather an artefact of the inversion process. The reason could be that the middle of the model time span is more constrained by the data, so that the end points are relatively more constrained by minimization of the L2 norm of the model parameters. This does however not

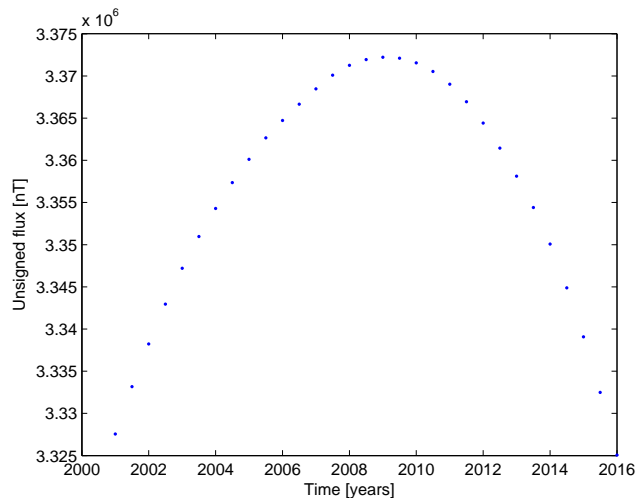


Figure 6.5: The change in the unsigned flux during the model time span.

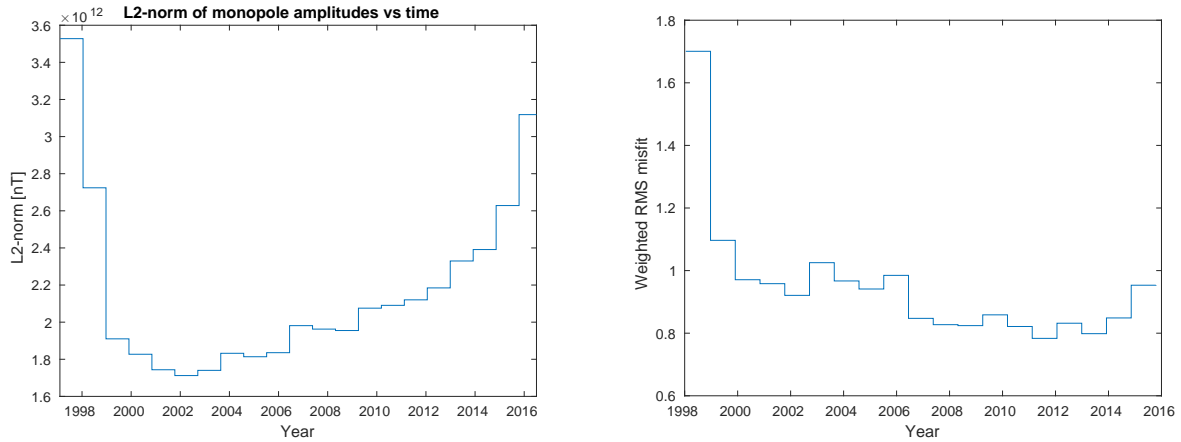


Figure 6.6: Left: Change in the L2-norm of the model parameters as a function of time. Right: Change in the weighted RMS misfit as a function of time.

seem to be the dominant cause, when looking at figure 6.6, as the L2-norm of the monopole amplitudes is lower in the middle of the time span. The misfit is much higher in 1998 to 2000, which is most likely due to the lack of satellite data during this time, so there is no clear trend in the misfit as a function of time.

The parabolic shape could however be because of how the time-dependence is modelled. A point in the middle of the time span will have a higher covariance with all the reference times, when compared to a point at the ends of the time span. Since monopole amplitudes are given weight according to the covariance of the reference times with the time that is being evaluated at, times in the middle of the model time span will give a higher mean weight to all of the monopoles compared to times at the end of the model time span. This could give rise to parabolic behaviour, see figure 6.7.

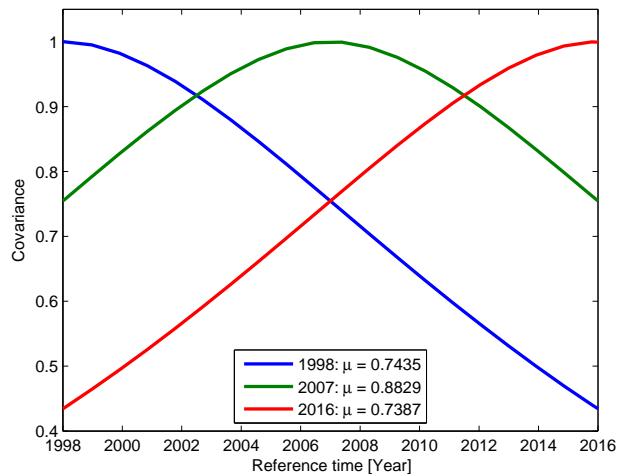


Figure 6.7: The covariance of the times 1998 (blue), 2007 (green) and 2016 (red) with the 22 reference times.  $\mu$  denotes the mean of the covariances.

An appropriate value for the characteristic time scale was found to be  $\tau = 6000$  days, which is approximately 16 years, almost equal to the entire model time span. This suggests that the time series of N could possibly be dominated by this "end effect", and a larger data set with a longer model time span would probably be less subjected to this problem, meaning that the actual change in unsigned flux is most likely even smaller than the 1.4 % that figure 6.5 suggests.

# Chapter 7

## Conclusion

In this thesis, a time-dependent core field model was made using ground observatory secular variation data, and satellite radial field component measurements from the CHAMP and Swarm missions. This model differs from most other main field models by using a monopole representation instead of spherical harmonics, and by modelling the time-dependence with covariance functions instead of splines. The reasoning behind choosing covariance function in place of splines for modelling the time-dependence, is that an appropriate choice of covariance function will allow for more "rough" time-dependence than splines, which produces very smooth time-dependence. It was hoped that the monopole representation, when combined with an L1-norm regularization of the radial field component at the core surface, would show interesting "sharp" and sparse structures that would usually be left unresolved by conventional L2 regularization. A time-dependent L1-regularization was however never successfully implemented, most likely due to problems with ill-conditioning of the design matrix that maps the monopole amplitudes to integration points on the core surface. Because of these difficulties, the results presented in this thesis have been made with an L2-norm regularization of the monopole amplitudes.

The results were overall in very good agreement with CHAOS-5 and CHAOS-6 models, producing very similar results with regards to the global secular variation, and also identified the same three pulses of secular acceleration at 2006, 2009 and 2013. When comparing fits to individual observatories, the covariance function approach to modelling time-dependence was still not able to capture the really fast changes in the SV measured at some observatories, but the general performance was quite good, sometimes even surpassing that of CHAOS-6, but the two models were very similar overall.

An investigation of the changes in the unsigned flux of the L2-regularized monopole model was also carried out. The time series showed a peculiar parabolic trend, which was interpreted as being due to the time-dependence modelling. Even with this artificial trend, the total change in the unsigned flux during the model time span of 16 years was low, only 1.4%. This change is not negligible, considering the time associated with the secular variation, but it is still noteworthy, considering that no attempts at constraining the change in unsigned flux was implemented in the inversion process.

There is still much work that can be done to improve this model. The most important problem that needs to be overcome is implementing the L1-regularization of the radial field at

the core surface in a time-dependent model. The static L1 model pictured in figure 5.8 shows a lot of new structure, and it would be very interesting to investigate in a time-dependent model. The problems plaguing the design matrix that relates monopole amplitudes to the Lebedev quadrature points at the core surface either need to be somehow resolved, or a new method of minimizing the L1-norm of the radial field component needs to be implemented.

There are other more minor things that could be improved. The observatory data sets reach back to 1998, but the first satellite measurements enter the data set with CHAMP near the end of the year 2000. This gap meant that the model was ill behaved prior to the year 2000, which could be remedied by including measurements from the Ørsted satellite.

The covariance function approach to modelling time-dependence is very flexible, and a more thorough investigation of different covariance functions and their hyperparameters might be able to improve the fits to observatory time series, so that the very fast changes visible at some observatories could be captured by the model.

# References

- Bloxham, J., & Gubbins, D. (1986). Geomagnetic field analysis-iv. testing the frozen-flux hypothesis. *Geophysical Journal International*, 84(1), 139-152. Retrieved from <http://gji.oxfordjournals.org/content/84/1/139.abstract> doi: 10.1111/j.1365-246X.1986.tb04349.x
- Chulliat, A., & Olsen, N. (2010). Observation of magnetic diffusion in the earth's outer core from magsat, Ørsted, and champ data. *Journal of Geophysical Research: Solid Earth*, 115(B5). Retrieved from <http://dx.doi.org/10.1029/2009JB006994> (B05105) doi: 10.1029/2009JB006994
- Constable, C. (1988). Parameter estimation in non-gaussian noise. *Geophysical Journal International*, 94(1), 131-142.
- Farquharson, C. G., & Oldenburg, D. W. (1998). Non-linear inversion using general measures of data misfit and model structure. *Geophysical Journal International*, 134(1), 213-227. Retrieved from <http://dx.doi.org/10.1046/j.1365-246x.1998.00555.x> doi: 10.1046/j.1365-246x.1998.00555.x
- Finlay, C. C., Olsen, N., Kotsiaros, S., Gillet, N., & Tøffner-Clausen, L. (2016). Recent geomagnetic secular variation from swarm and ground observatories as estimated in the chaos-6 geomagnetic field model. *Earth, Planets and Space*, 68(1), 1-18. Retrieved from <http://dx.doi.org/10.1186/s40623-016-0486-1> doi: 10.1186/s40623-016-0486-1
- Finlay, C. C., Olsen, N., & Tøffner-Clausen, L. (2015). Dtu candidate field models for igrf-12 and the chaos-5 geomagnetic field model. *Earth, Planets and Space*, 67(1), 1.
- Friis-Christensen, E., Lühr, H., & Hulot, G. (2006). Swarm: A constellation to study the earth's magnetic field. *Earth, Planets and Space*, 58(4), 351-358. Retrieved from <http://dx.doi.org/10.1186/BF03351933> doi: 10.1186/BF03351933
- Garland, G. D. (1979). The contributions of carl friedrich gauss to geomagnetism. *Historia Mathematica*, 6(1), 5-29.
- Gillet, N., Jault, D., Finlay, C., & Olsen, N. (2013). Stochastic modeling of the earth's magnetic field: inversion for covariances over the observatory era. *Geochemistry, Geophysics, Geosystems*, 14(4), 766-786.
- Huber, P. J. (1964, 03). Robust estimation of a location parameter. *Ann. Math. Statist.*, 35(1), 73-101. Retrieved from <http://dx.doi.org/10.1214/aoms/1177703732> doi: 10.1214/aoms/1177703732
- Jackson, A., Constable, C. G., Walker, M. R., & Parker, R. L. (2007). Models of earth's main magnetic field incorporating flux and radial vorticity constraints. *Geophysical Journal International*, 171(1), 133-144. Re-

- trieved from <http://gji.oxfordjournals.org/content/171/1/133.abstract> doi: 10.1111/j.1365-246X.2007.03526.x
- Jackson, A., & Finlay, C. (2015). Geomagnetic secular variation and its applications to the core. In G. Schubert (Ed.), *Treatise on geophysics*. Amsterdam: Elsevier. Retrieved from <http://www.sciencedirect.com/science/article/pii/B9780444527486000870> doi: <http://dx.doi.org/10.1016/B978-044452748-6.00087-0>
- Jackson, A., Jonkers, A. R. T., & Walker, M. R. (2000). Four centuries of geomagnetic secular variation from historical records. *Philosophical Transactions of the Royal Society of London A: Mathematical, Physical and Engineering Sciences*, 358(1768), 957–990. Retrieved from <http://rsta.royalsocietypublishing.org/content/358/1768/957> doi: 10.1098/rsta.2000.0569
- Jones, C. (2007). Geodynamo. In D. Gubbins & E. Herrero-Bervera (Eds.), *Encyclopedia of geomagnetism and paleomagnetism*. Netherlands: Springer.
- Kother, L., Hammer, M., Finlay, C., & Olsen, N. (2015). An equivalent source method for modelling the global lithospheric magnetic field. *Geophysical Journal International*, 203, 553–566. doi: 10.1093/gji/ggv317
- Lebedev, V., & Laikov, D. (1999). A quadrature formula for the sphere of the 131st algebraic order of accuracy. In *Doklady. mathematics* (Vol. 59, pp. 477–481).
- Leopardi, P. (2006). A partition of the unit sphere into regions of equal area and small diameter. *Electronic Transactions on Numerical Analysis*, 25(12), 309–327.
- Matzka, J., Chulliat, A., Manda, M., Finlay, C. C., & Qamili, E. (2010). Geomagnetic observations for main field studies: From ground to space. *Space Science Reviews*, 155(1), 29–64. Retrieved from <http://dx.doi.org/10.1007/s11214-010-9693-4> doi: 10.1007/s11214-010-9693-4
- Maus, S. (2007). Champ. In D. Gubbins & E. Herrero-Bervera (Eds.), *Encyclopedia of geomagnetism and paleomagnetism*. Netherlands: Springer.
- O’Brien, M. S., & Parker, R. L. (1994). Regularized geomagnetic field modelling using monopoles. *Geophysical Journal International*, 118(3), 566–578. Retrieved from <http://dx.doi.org/10.1111/j.1365-246X.1994.tb03985.x> doi: 10.1111/j.1365-246X.1994.tb03985.x
- Olsen, N., & Finlay, C. (2015). Lecture notes for geomagnetism course.
- Olsen, N., Hulot, G., & Sabaka, T. J. (2010). Measuring the earth’s magnetic field from space: Concepts of past, present and future missions. *Space Science Reviews*, 155(1), 65–93. Retrieved from <http://dx.doi.org/10.1007/s11214-010-9676-5> doi: 10.1007/s11214-010-9676-5
- Olsen, N., Hulot, G., & Sabaka, T. J. (2014). Sources of the geomagnetic field and the modern data that enable their investigation. In W. Freedman, M. Zuhair Nashed, & T. Sonar (Eds.), *Handbook of geomathematics*. Springer.
- Olsen, N., Lüher, H., Finlay, C. C., Sabaka, T. J., Michaelis, I., Rauberg, J., & Tøffner-Clausen, L. (2014). The chaos-4 geomagnetic field model. *Geophysical Journal International*, 197(2), 815–827.
- Rasmussen, C. E., & Williams, C. K. I. (2006). *Gaussian processes for machine learning*. The MIT Press.
- Schumaker, L. (2007). *Spline functions: basic theory*. Cambridge University Press.

- Stern, D. P. (2002). A millennium of geomagnetism. *Reviews of geophysics*, 40(3).
- Thébault, E., Purucker, M., Whaler, K. A., Langlais, B., & Sabaka, T. J. (2010). The magnetic field of the earth's lithosphere. *Space Science Reviews*, 155(1), 95–127. Retrieved from <http://dx.doi.org/10.1007/s11214-010-9667-6> doi: 10.1007/s11214-010-9667-6
- Wardinski, I., & Lesur, V. (2012). An extended version of the c3fm geomagnetic field model: application of a continuous frozen-flux constraint. *Geophysical Journal International*, 189(3), 1409-1429. Retrieved from <http://gji.oxfordjournals.org/content/189/3/1409.abstract> doi: 10.1111/j.1365-246X.2012.05384.x

# Appendix A

## Matlab code

Three of the important MatLab codes used through the thesis are listed here, starting with an example of a how a time-dependent design matrix for satellite data is computed. Then follows the code for performing an L2-regularized inversion, and finally the code for the (static) L1-regularized inversion, which was used in determining the appropriate monopole grid parameters.

### A.1 Time-dependent design matrix

```
1 % Define Constants
2 a = 6371.2; % earth radius
3 c=3480.0; % core radius
4 rad = pi/180;
5 deg = 180/pi;
6 params.depth = 0.625*a; % depth of monopoles [km] ...
   measured downward from surface
7 params.mono_rad = a - params.depth; % Monopole radius [km]
8 dim=2; % dimension for EQSP algorithm
9 N=500; % Number of monopoles for EQSP ...
   algorithm
10 n_m=N;
11
12 % Read data file
13 filename = '../Data/CHAMP_10min_dark_quiet_NEC.dat';
14 N_Data_Step = 1; % 1/N_data.Step is the fraction of the data to be used
15 delimiterIn = ' ';
16 headerlinesIn = 2;
17 temp = importdata(filename,delimiterIn,headerlinesIn);
18
19 %locations
20 t_d=temp.data(1:N_Data_Step:end,1); % data times
21 t_m=dlmread('tm.22.mat'); % vector of reference times
22 n_tm=length(t_m); % number of reference times
23 n_d=length(t_d); % number of data points
24
25 r=temp.data(1:N_Data_Step:end,2); % radial coordinates
```

```

26 theta=temp.data(1:N_Data_Step:end,3); % latitude
27 lambda=temp.data(1:N_Data_Step:end,4); % longitude
28 sin_theta = sind(theta);
29 cos_theta = cosd(theta);
30
31
32 % Setup Monopole grid using EQSP
33 points = eq_point_set(dim,N); % Get Cartesian coordinates of monopole ...
    grid points
34 points_x=points(1,:);
35 points_y=points(2,:);
36 points_z=points(3,:);
37
38 % Convert to spherical coordinates
39 Monopole.lambda=atan2(points_x,points_y).*deg;
40 Monopole.theta=acosd(points_z./sqrt(points_x.^2+points_y.^2+points_z.^2));
41 Monopole.sin_theta = sind(Monopole.theta);
42 Monopole.cos_theta = cosd(Monopole.theta);
43 Monopole.rad = (params.mono_rad)*ones(N,1);
44
45 % Calculation of Design matrix
46 disp('Calculation of Design matrix')
47
48 % Setup hyperparameters for GPML script
49 d=3; % \ny
50 sf=1; % signal variance
51 ell=6000; % \tau in days
52
53 hyp = [ log(ell)
54 log(sf) ];
55
56 K=covMaterniso(d,hyp,t_d,t_m); % Calculate covariance matrix (Matern)
57 Gr=NaN*ones(n_d,n_m*n_tm);
58
59 % Calculate the design matrix
60 for i = 1:n_d
61
62 cos_mu = cos_theta(i).*Monopole.cos_theta + ...
    sin_theta(i).*Monopole.sin_theta.*cosd(lambda(i)-Monopole.lambda);
63 dist = sqrt(Monopole.rad.^2+r(i).^2-(2.*r(i).*Monopole.rad.*cos_mu));
64 for j = 1:n_tm
65 Gr(i,(j-1)*n_m+1:(j-1)*n_m+n_m) = ((r(i) - ...
    Monopole.rad.*cos_mu)./(dist.^3)).*K(i,j);
66 end
67
68 end

```

## A.2 L2-regularized inversion

```

1 % Setup file names for pre-computed design matrices
2 G_r = 'Gr_SV_Matern.N500.L6000.mat ';
3 G_theta = 'Gtheta_SV_Matern.N500.L6000.mat ';

```

```

4   G_lambda= 'Glambda_SV_Matern_N500_L6000.mat';
5   G_champ1 ='Gr_CHAMP_Matern_N500_L6000_1.mat';
6   G_champ2 ='Gr_CHAMP_Matern_N500_L6000_2.mat';
7   G_SW_A   = 'Gr_Swarm_A_Matern_N500_L6000.mat';
8   G_SW_B   = 'Gr_Swarm_B_Matern_N500_L6000.mat';
9   G_SW_C   = 'Gr_Swarm_C_Matern_N500_L6000.mat';
10
11  % Collect them in a list
12  G_list=[G_r; G_theta; G_lambda; G_champ1; G_champ2; G_SW_A; G_SW_B; ...
13         G_SW_C];
14
15  % File names for the satellite data files
16  filename=['../Data/CHAMP_10min_dark_quiet_NEC1.dat'
17           '../Data/CHAMP_10min_dark_quiet_NEC2.dat'
18           '../Data/SW_A_10min_dark_quiet_NEC.txt  '
19           '../Data/SW_B_10min_dark_quiet_NEC.txt  '
20           '../Data/SW_C_10min_dark_quiet_NEC.txt  '];
21  filename=cellstr(filename);
22
23  % Setup CHAOS-6 model
24  load ('CHAOS-6.mat')
25  options.filename_apexsh = 'apexsh_1980-2020.txt';
26  N = 14;
27  pp_N = pp;
28  pp_N.dim = N*(N+2);
29  coefs_tmp = reshape(pp.coefs, [], pp.pieces, pp.order);
30  pp_N.coefs = reshape(coefs_tmp(1:N*(N+2),:,:), [], pp.order);
31
32  % Set constants
33  a=6371.2;
34  rad=pi/180;
35  n_m=500;
36  n_tm=22;
37
38  % Here satellite data files are loaded up 1 by 1 and the prior covariance
39  % estimates are calculated according to QD-latitude
40  disp('Load satellite data and create prior variance estimates')
41  Cv_sat=NaN*ones(34711,length(filename));           % Pre-allocating ...
42  % the size of these vectors
43  d_sat=NaN*ones(34711,length(filename));
44  theta_sat=NaN*ones(34711,length(filename));
45  QD_lat_sat=NaN*ones(34711,length(filename));
46  for j=1:length(filename)
47  N_Data_Step = 1; % 1/N_data_Step is the fraction of the data to be used
48  delimiterIn = ' ';
49  headerlinesIn = 2;
50  temp = importdata(char(filename(j)),delimiterIn,headerlinesIn); % load ...
51  % data file
52  t=temp.data(1:N_Data_Step:end,1);
53  r=temp.data(1:N_Data_Step:end,2);
54  theta=temp.data(1:N_Data_Step:end,3);
55  theta_sat(1:length(t),j)=theta;
56  phi=temp.data(1:N_Data_Step:end,4);

```

```

55     d_sat(1:length(t),j)=temp.data(1:N_Data_Step:end,14);           % save ...
        radial core-field component as column in d_sat
56     B_core = synth_values(r, theta, phi, pp_N, t);                 % Get ...
        CHAOS-6 prediction
57     B_core = B_core(:,1);
58     dB_rtp=d_sat(~isnan(d_sat(:,j)),j)-B_core;                    % residual ...
        of measurement with CHAOS-6 prediction
59     QD_lat = qdipole(t, r/a, theta*rad, (phi+180)*rad, ...
        options.filename_apexsh); % Convert to QD_latitude
60     QD_lat_sat(1:length(t),j) = QD_lat;
61     QD_lat_bins = [-90:5:90]';                                     % make bins ...
        of QD_latitude
62     B_sigma = zeros(length(QD_lat_bins)-1, 1);
63
64     for k = 1:length(QD_lat_bins)-1
65         index = find(QD_lat_bins(k) < QD_lat(:,1) & QD_lat(:,1) < ...
            QD_lat_bins(k+1)); % Find measurements in bins
66         [dF_mean, B_sigma(k,1)] = huber(dB_rtp(index, 1));        % Output sigma ...
            from Huber routine
67     end
68
69     sigma_B_rtp = interp1((QD_lat_bins(1:end-1)+QD_lat_bins(2:end))/2, ...
        B_sigma, QD_lat, 'spline'); % Interpolate values between bin centres
70     Cv_sat(1:length(t),j)=1./(sigma_B_rtp.^2); % Calculate the inverse of ...
        the covariances
71     end
72     clear temp sigma_B_rtp dF_mean B_sigma t r phi B_core dB_rtp
73
74     disp('Load observatory data and create prior variance estimates')
75
76     % Load observatory data
77     load('obsdata.mat');
78     dB_r=dB_obs_all(:,1);
79     dB_theta=dB_obs_all(:,2);
80     dB_lambda=dB_obs_all(:,3);
81     [obs_list,ia,ic]=unique(obs_all,'rows');
82
83     % Collect all measurements in one array
84     d_obs=NaN*ones(34711,3);
85     d_obs(1:length(dB_r),1)=dB_r;
86     d_obs(1:length(dB_theta),2)=dB_theta;
87     d_obs(1:length(dB_lambda),3)=dB_lambda;
88     d=[d_obs d_sat];
89
90     % Collect all prior covariance estimates in one array
91     Cv_r=C_1_11;
92     Cv_theta=C_1_22;
93     Cv_lambda=C_1_33;
94     Cv_obs=NaN*ones(34711,3);
95     Cv_obs(1:length(Cv_r),1)=Cv_r;
96     Cv_obs(1:length(Cv_theta),2)=Cv_theta;
97     Cv_obs(1:length(Cv_lambda),3)=Cv_lambda;
98     Cv=[Cv_obs Cv_sat];
99     clear Cv_r Cv_theta Cv_lambda d_obs d_sat dB_r dB_theta dB_lambda

```

```

100
101 % Calculate GtG and Gtd
102 disp('Iteratively determining weights, GtG and Gtd')
103 huber=NaN*ones(34711,length(G_list));
104 GtG=zeros(n_m*n_tm);
105 Gtd=zeros(n_m*n_tm,1);
106 alpha_reg_l2=4.641610e-23; % Regularization parameter
107 k_lim=10;
108 Ig=eye(n_m*n_tm);
109 k=0;
110 delta_norm=100;
111 res=NaN*ones(34711,length(G_list));
112
113 for j=1:length(G_list)
114 G=load(char(G_list(j))); % Load a G-matrix
115 G=struct2cell(G);
116 G=cell2mat(G);
117 C=Cv(~isnan(Cv(:,j)),j); % Select the corresponding column in array of ...
    covariance estimates and remove NaN
118 D=d(~isnan(d(:,j)),j); % Select the corresponding column in array of ...
    data and remove NaN
119
120 GtG = GtG + G'*diag(C)*G; % Calculate GtG and GtD
121 Gtd = Gtd + G'*diag(C)*D;
122 end
123
124 m_l2=(GtG+alpha_reg_l2*Ig)\Gtd; % Initial model parameters to start ...
    iteration
125
126 while delta_norm > 1e-3
127 GtG=zeros(n_m*n_tm); % Clear GtG and Gtd
128 Gtd=zeros(n_m*n_tm,1);
129 k=k+1;
130 for j=1:length(G_list)
131 G=load(char(G_list(j))); % Load G-matrix again
132 G=struct2cell(G);
133 G=cell2mat(G);
134 C=Cv(~isnan(Cv(:,j)),j); % Get covariance vector again
135 D=d(~isnan(d(:,j)),j); % Get data vector again
136 res(1:length(D),j)=D-G*m_l2(:,k); % Calculate residuals
137 misfit_rms(j)=nanstd(res(:,j)); % Get RMS value of residuals
138 huber=min((1.5.*sqrt(1./C))./abs(res(~isnan(res(:,j)),j)),1); % ...
    Calculate the huber weights
139 meanhuber(j)=mean(huber); % Get mean of huber weights
140 W=diag(huber.*C); % Calculate diagonal weighting matrix
141 mis(j)=res(~isnan(res(:,j)),j)'*W*res(~isnan(res(:,j)),j); % Get ...
    weighted misfit
142 N(j)=length(D); % Number of data ...
    points in set
143 GtG = GtG + G'*W*G; % Calculate GtG
144 Gtd = Gtd + G'*W*D; % And Gtd
145 end
146 m_l2(:,k+1)=(GtG+alpha_reg_l2*Ig)\Gtd; % Calculate model parameters

```

```

147 delta_norm=abs((norm(m_l2(:,k+1))-norm(m_l2(:,k)))/norm(m_l2(:,k))) ...
      % And the convergence criteria
148 if k > k_lim
149 delta_norm
150 delta_norm = 1e-4;
151 end
152 end
153 k           % output some diagnostics
154 delta_norm
155 meanhuber
156 misfit_rms
157 m_l2=m_l2(:,end);           % Set m to be the converged m
158 l2_norm=norm(m_l2)         % Get the L2-norm
159 total_misfit=sqrt(sum(mis)/sum(N))           % And the total weighted RMS ...
      misfit
160 R=(GtG+alpha_reg_l2*Ig)\GtG;           % Calculate resolution matrix
161 Cm=(sum(mis)/sum(N-trace(R)))*(GtG+alpha_reg_l2*Ig)\eye(n_m*n_tm); % ...
      And model covariance matrix

```

### A.3 Static L1-regularized inversion

```

1 alpha_reg_l2=2.6367e-09; % L2 and L1 damping parameters
2 alpha_reg_l1=0.0034;
3
4 % Define Constants
5 a = 6371.2;
6 c=3480.0;
7 rad = pi/180;
8 deg = 180/pi;
9 load 'coast.mat';
10
11 params.depth = 0.625*a;           % depth of monopoles [km] ...
      measured downward from surface
12 params.mono_rad = a - params.depth; % Monopole radius [km]
13 dim=2;
14 N=600;
15
16 % Read data file
17 filename = '../Data/SW_A.FEB15a.NEC.dark';
18 N_Data_Step = 100; % 1/N_data.Step is the fraction of the data to be used
19 delimiterIn = ' ';
20 headerlinesIn = 2;
21 temp = importdata(filename,delimiterIn,headerlinesIn);
22
23 %locations
24 t=temp.data(1:N_Data_Step:end,1);
25 r=temp.data(1:N_Data_Step:end,2);
26 theta=temp.data(1:N_Data_Step:end,3);
27 lambda=temp.data(1:N_Data_Step:end,4);
28 sin_theta = sind(theta);
29 cos_theta = cosd(theta);
30

```

```

31 % Observations
32 Br_all=temp.data(1:N_Data_Step:end,5);
33 Btheta_all=temp.data(1:N_Data_Step:end,6);
34 Blambda_all=temp.data(1:N_Data_Step:end,7);
35
36 %Crustal estimate
37 Br_crust=temp.data(1:N_Data_Step:end,8);
38 Btheta_crust=temp.data(1:N_Data_Step:end,9);
39 Blambda_crust=temp.data(1:N_Data_Step:end,10);
40
41 % External estimate
42 Br_ext=temp.data(1:N_Data_Step:end,11);
43 Btheta_ext=temp.data(1:N_Data_Step:end,12);
44 Blambda_ext=temp.data(1:N_Data_Step:end,13);
45
46 % Corrected observations
47 Br=Br_all-Br_crust-Br_ext;
48 Btheta=Btheta_all-Btheta_crust-Btheta_ext;
49 Blambda=Blambda_all-Blambda_crust-Blambda_ext;
50
51 % Setup Monopole grid using EQSP
52 points = eq_point_set(dim,N);
53 points_x=points(1,:);
54 points_y=points(2,:);
55 points_z=points(3,:);
56
57 Monopole.lambda=atan2(points_x,points_y).*deg;
58 Monopole.theta=acosd(points_z./sqrt(points_x.^2+points_y.^2+points_z.^2));
59 Monopole.sin_theta = sind(Monopole.theta);
60 Monopole.cos_theta = cosd(Monopole.theta);
61 Monopole.rad = (params.mono_rad)*ones(N,1);
62
63 % Calculation of static Design matrices
64 disp('Calculation of Design matrix')
65
66 for i = 1:length(lambda)
67
68     cos_mu = cos_theta(i).*Monopole.cos_theta + ...
69         sin_theta(i).*Monopole.sin_theta.*cosd(lambda(i)-Monopole.lambda);
70     dist = ...
71         sqrt(Monopole.rad.^2+r(i).^2-(2.*r(i).*Monopole.rad.*cos_mu));
72     Gr(i,:) = ((r(i) - Monopole.rad.*cos_mu)./(dist.^3))';
73     Gtheta(i,:) = ...
74         ((Monopole.rad.*(sin_theta(i).*Monopole.cos_theta - ...
75             cos_theta(i).*Monopole.sin_theta.*cosd(lambda(i)-Monopole.lambda))./(dist.^3))');
76     Glambda(i,:) = ...
77         ((Monopole.rad.*Monopole.sin_theta.*sind(lambda(i)-Monopole.lambda))./(dist.^3))';
78 end
79
80 % Matrices and vectors needed for regularized inversion
81 G=[Gr ; Gtheta ; Glambda];
82 d=[Br; Btheta; Blambda];
83 Gt=G';
84 GtG=Gt*G;

```

```

80     Gtd=Gt*d;
81
82     % Making L2-solution
83     Ig=Gr_inv'*Gr_inv;
84     w_l2=ones(size(d));
85     W_l2=diag(w_l2);
86     m_l2(:,1)=ones(N,1);
87
88     %% inversion for l2 model parameters
89
90     for j=1:10
91         m_l2(:,j+1)=(Gt*W_l2*G+alpha_reg_l2*Ig)\Gt*W_l2*d;
92
93         Br_pred_l2      = Gr*m_l2(:,j+1);
94         Btheta_pred_l2 = Gtheta*m_l2(:,j+1);
95         Blambda_pred_l2 = Glambda*m_l2(:,j+1);
96
97         d_pred_l2=[Br_pred_l2; Btheta_pred_l2; Blambda_pred_l2];
98         res_l2=d-d_pred_l2;
99
100        sigma_l2=sqrt(res_l2'*res_l2/length(res_l2));
101        w_l2=min(1.5*sigma_l2./abs(res_l2),1);
102        W_l2=diag(w_l2);
103    end
104    m_l2=m_l2(:,end);
105
106    % Making L1-solution
107    eps=1;          % Epsilon for Ekbloms measure
108
109    % Assigning L2-solution as starting model
110    m_l1(:,1)=m_l2;
111    Rx=diag(w_leb.*((Gr_inv*m_l2).^2+eps^2).^-(1/2));
112    l1_change=1;
113    k=0;
114    w=ones(size(d));
115    W=diag(w);
116
117    %% inversion for L1 model parameters
118    while l1_change > 10^-3
119        k=k+1;
120
121        m_l1(:,k+1)=(Gt*W*G+alpha_reg_l1*Gr_inv'*Rx*Gr_inv)\Gt*W*d;
122        Rx=diag((Gr_inv*m_l1(:,k+1)).^2+eps^2)^-(1/2);
123
124        Br_pred_l1      = Gr*m_l1(:,k+1);
125        Btheta_pred_l1 = Gtheta*m_l1(:,k+1);
126        Blambda_pred_l1 = Glambda*m_l1(:,k+1);
127        d_pred_l1=[Br_pred_l1; Btheta_pred_l1; Blambda_pred_l1];
128
129        res_l1=d-d_pred_l1;
130        w=min(1.5*sigma_l2./abs(res_l1),1);
131        W=diag(w);
132
133        l1_change=sum(abs(m_l1(:,k+1)-m_l1(:,k)))/sum(abs(m_l1(:,k)))

```

```
134     change=l1_change;  
135  
136     if k > 199  
137  
138         l1_change=10^-4;  
139         limit=1;  
140         disp('Iteration number limit reached')  
141     end  
142  
143 end
```

**DTU Space**

National Space Institute  
Technical University of Denmark

Elektrovej, building 327  
DK - 2800 Kgs. Lyngby  
Tel (+45) 4525 9500  
Fax (+45) 4525 9575

[www.space.dtu.dk](http://www.space.dtu.dk)